PHYSICAL REVIEW B **100**, 035303 (2019)

Effect of hexagonal warping of the Fermi surface on the thermoelectric properties of a topological insulator irradiated with linearly polarized radiation

Tarun Choudhari and Nivedita Deo[*]
Department of Physics and Astrophysics, University of Delhi, Delhi-110007, India

(Received 27 January 2018; revised manuscript received 13 May 2019; published 8 July 2019)

We investigate the effect of the hexagonal warped anisotropic Fermi surface on the anomalous thermoelectric properties of the topological insulator surface illuminated with linearly polarized off-resonant electromagnetic radiation. Upon irradiation of the TI surface, the linearly polarized (LP) off-resonant radiation couples with the Dirac surface states. By explicitly finding the off-resonant quasistatic Hamiltonian we show that this coupling occurs only in the presence of the hexagonal warping of the Fermi surface of the topological insulator. We calculate the spin texture of the surface states, Berry curvature, Berry phase, orbital magnetic moment, and magnetization associated with the band structure, which we find strongly depends on the angle of polarization and the amplitude of radiation. For the anomalous thermoelectric effects generated by the Berry curvature, it is found that due to the hexagonal warping induced Fermi surface deformation and the radiation parameter dependent spin texture of the surface states, the transverse Hall, Ettingshausen, Nernst, and thermal conductivities show significant variation with the change in polarization angle, chemical potential, temperature, and the amplitude of radiation. As a consequence, the thermoelectric coefficient of performance (ZT) of the topological insulator is found to be increased in the presence of LP off-resonant irradiation compared to the absence of radiation.

DOI: 10.1103/PhysRevB.100.035303

I. INTRODUCTION

The topological insulator surface when irradiated with time periodic electromagnetic radiation exhibits a type of surface states called the Floquet-Dirac states [1–5]. This is just like the space translation symmetry induced Bloch states of the electron in crystalline solids. The Floquet-Dirac states are a consequence of the minimal coupling of Dirac electron momentum with the time periodic vector potential of radiation which leads to a time periodic electron Hamiltonian on the surface of the topological insulator. The existence of these states in the topological insulator has been verified both theoretically [1–3] and experimentally using the time- and angle-resolved photoemission spectroscopy [6]. Due to the existence of Floquet-Dirac states, the topological insulator exhibits radiation polarization controllable photocurrent [7–10], which is induced by the photodrag effect in the case of the topological insulator having center of inversion symmetry (i.e., centrosymmetric) [8] and photogalvanic effect in the case of noncentrosymmetric TI [8–10]. In the photodrag effect, the photocurrent on the surface of the irradiated topological insulator is generated by the in-plane component of the photon momentum, whereas the photogalvanic effect is induced by the out-of-plane component of the photon momentum [8]. In particular, the off-resonant (i.e., the photon energy of radiation is much greater than the energy bandwidth of TI) illumination of a topological insulator surface with circular polarized light (CPL), generates a CPL helicity dependent time reversal symmetry breaking mass term [11–14] in the quasistatic effective Hamiltonian of the Floquet-Dirac states. This causes the topological insulator to fall into the Floquet-Chern phase characterized by the Floquet-Chern number, a topological invariant [3,12]. The interface of two such distinct Floquet-Chern insulators hosts one-dimensional (1D) spin polarized chiral states [12]. The CPL irradiation also leads to a CPL helicity dependent spin polarized current [15,16], circular photogalvanic effect [17], and anomalous Ettingshausen and Nernst thermomagnetic effects in graphene and topological insulators [13,14]. The anomalous Ettingshausen thermomagnetic effect generates a transverse heat current on the application of a longitudinal electric field on the surface of the topological insulator, whereas in an anomalous Nernst thermomagnetic effect a transverse electric current is generated by a temperature gradient [14]. The anomalous thermoelectric currents are induced by the nonzero Berry curvature and Berry curvature corrected nonzero orbital magnetization generated by the self-rotation of the Dirac electron wave packet around its center [18], this is in contrast to normal Ettingshausen and Nernst currents which instead of nonzero Berry curvature occur due to the presence of nonzero magnetic field in the system [19].

Besides these effects, both theoretical calculations and angle-resolved photoemission spectroscopy (ARPES) experiments reveal that the circular Fermi surface of the low energy spectrum (Dirac cone) of the surface states in the Bi-chalcogenides topological insulators like Bi_2Se_3, Bi_2Te_3, and Sb_2Te_3 attain a snowflakelike shape at high energy. This warping of Fermi surface occurs due to the presence of a C_{3v} rotational symmetric k-cubic hexagonal warping term (i.e., $k_x^3 - 3k_y^2k_x$) in the Hamiltonian of the Bi-chalcogenides topological insulator exhibiting a C_{3v} rotational symmetry in the bulk [20–22]. The k-cubic hexagonal warping term

---

[*] ndeo007@gmail.com

due to its anisotropic nature in momentum space causes anisotropic orbital coupling of the electron momentum with the electromagnetic radiation vector potential. This leads to the spin shift current [23] in the Bi-chalcogenides topological insulator irradiated with polarized radiation, change in the optical absorption and the degree of circular dichroism [24], and a nonzero photocurrent [7] (which is otherwise zero in the absence of hexagonal warping).

In this paper we investigate the effect of this anisotropic hexagonal warping of Fermi surface on the anomalous transverse Nernst, Ettingshausen, and thermal conductivities for the Bi-chalcogenides topological insulator surface irradiated with linearly polarized electromagnetic radiation in the off-resonant regime (i.e., the photon energy of radiation is much greater than the bandwidth of TI). Previously, these thermoelectric properties of the topological insulator have been studied for the circular Fermi surface of the energy band, i.e., at low energy of the Dirac electron, for the off-resonant circularly polarized electromagnetic irradiation of the surface of TI [13,14]. However, a study of the linearly polarized off-resonant irradiation in the presence of an anisotropic hexagonally warped Fermi surface has not been done. We show here that the hexagonal warping of the Fermi surface makes the transverse anomalous Nernst and Ettingshausen thermoelectric effect dependent upon the amplitude and angle of polarization of the linearly polarized radiation and this dependence is absent when there is no hexagonal warping of the Fermi surface.

This paper is organized as follow. In Sec. II we derive the off-resonant quasistatic Hamiltonian and the spin texture for the Floquet-Dirac states for the linearly polarized (LP) irradiation of TI. We calculate the Berry curvature, Berry phase and anomalous Hall conductivity in Sec. III, and orbital magnetic moment and magnetization in Sec. IV. We then find the anomalous transverse thermoelectric conductivities for the LP irradiation of TI in Sec. V and the figure of merit in Sec. VI.

II. BASIC FORMALISM AND MODEL FOR AN OFF-RESONANT IRRADIATED TOPOLOGICAL INSULATOR

A. Floquet Hamiltonian and the surface states

We consider a Bi_2Se_3 topological insulator (001) surface irradiated perpendicularly with linearly polarized light having polarization at angle θ with respect to the x axes (Fig. 1). The linearly polarized electromagnetic radiation is described by the time varying vector potential

$$\vec{A}_{xy}(t) = A_x(t)\hat{x} + A_y(t)\hat{y} = \frac{E_o}{\omega}\cos\omega t\,(\cos\theta\hat{x} + \sin\theta\hat{y}). \quad (1)$$

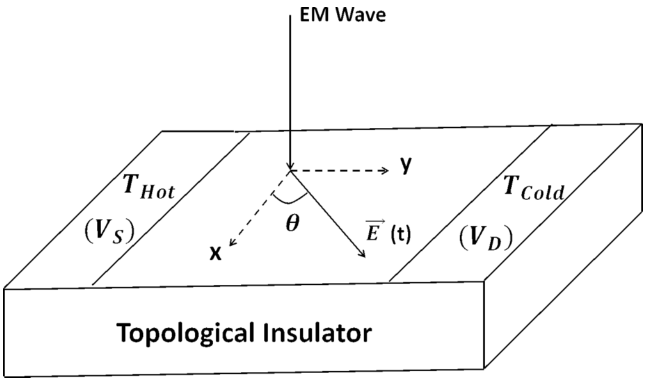

FIG. 1. Schematic of the topological insulator surface irradiated with linearly polarized electromagnetic radiation.

The E_o, ω, and θ in the above equation are the amplitude of the electric field vector, the angular frequency of the electromagnetic radiation, and the angle between the x axes and the electric field vector of the electromagnetic radiation, respectively. The surface states of the Bi-chalcogenide topological insulator with nonzero hexagonal warping of the Fermi surface is described by the following Fu-model Hamiltonian [20]:

$$\mathcal{H}_o = \hbar v_{xy}(\sigma_x k_y - \sigma_y k_x) + \lambda_h\big(k_x^3 - 3k_y^2 k_x\big)\sigma_z + \Delta\sigma_z. \quad (2)$$

In Eq. (2), $v_{xy} \approx 0.4 \times 10^6$ m/s [20–22] defines the Fermi velocity and $\lambda_h = 0.250$ eV nm^3 [20–22] (for Bi_2Se_3) defines the hexagonal warping parameter for the C_3 rotational symmetric anisotropic k-cubic hexagonal warping term (i.e., $k_x^3 - 3k_y^2 k_x$). This hexagonal warping term of the surface state Hamiltonian [Eq. (2)] is a result of C_3 rotational symmetry present in the bulk of the three-dimensional (3D) Bi-chalcogenide topological insulators [20–22]. Δ is the band gap parameter, which originates due to the quantum tunneling between the surface states residing at the bottom and top surface of the 3D topological insulator film [25,26]. This band gap varies with the thickness of the topological insulator film, and for Bi_2Se_3 it lies between 0.041 and 0.252 eV [26] for the film thickness of 5 to 2 quintuple layers (QL), respectively. For numerical calculations we choose $\Delta = 70$ meV which corresponds to an ultrathin topological insulator film of thickness around 3QL [26]. On irradiation of the topological insulator surface with linearly polarized radiation, the vector potential $\vec{A}_{xy}(t)$ [Eq. (1)] couples with the momentum of the Dirac electron via Peierls substitution $\vec{p} \to (\vec{p} - e\vec{A})$ and makes the Hamiltonian time dependent. By using this Peierls substitution in the surface state Hamiltonian given in Eq. (2), we find the following time dependent Hamiltonian for the surface states of the topological insulator:

$$\mathcal{H}(t) = \hbar v_{xy}[\sigma_x k_y(t) - \sigma_y k_x(t)] + \Delta\sigma_z + \lambda_h\big[k_x^3(t) - 3k_y^2(t)k_x(t)\big]\sigma_z, \quad (3)$$

where $k_x(t) = (k_x + \frac{eA_x(t)}{\hbar})$ and $k_y(t) = (k_y + \frac{eA_y(t)}{\hbar})$. In Eq. (3), due to the weak value of $\vec{B}(t)$, we have not taken into account the Zeeman coupling which arises due to the coupling of the Dirac electron spin and the time varying magnetic field $[\vec{B}(t)]$ of the electromagnetic radiation. For the electric field amplitude of order $E_0 \approx 10^9$ V/m, the magnetic field amplitude of the electromagnetic radiation will be of the order of $B_0 \approx 10$ T, this magnetic field leads to a gap generating the Zeeman term in the Hamiltonian of the order of $\mu_B g B_0 \approx 0.001$ eV (where $\mu_B \approx 5.78 \times 10^{-5}$ eV T^{-1} is the Bohr magneton and $g \approx 2$ is the Landé g factor). On comparing the Zeeman term with the band gap $\Delta = 0.07$ eV in the problem studied, the energy band gap is negligibly altered by the Zeeman term, hence the effect of the magnetic field can be safely ignored in the Hamiltonian [Eq. (3)]. Now, using Eq. (1), the Hamiltonian of Eq. (3) can be written as

$$\mathcal{H}(t) = \mathcal{H}_o + \mathcal{H}_p(t), \tag{4}$$

where $\mathcal{H}_o$ is the time independent part of Hamiltonian $\mathcal{H}(t)$, given by Eq. (2) and $\mathcal{H}_p(t)$ is the time dependent part of Hamiltonian $\mathcal{H}(t)$, given by

$$\begin{aligned}\mathcal{H}_p(t) = {} & a\hbar v_{xy}(\sin\theta\sigma_x - \cos\theta\sigma_y) + \lambda_h\{a^3\cos^3\omega t\cos 3\theta \\ & + 3a^2\cos^2\omega t(\cos 2\theta k_x - \sin 2\theta k_y) \\ & + 3a\cos\omega t[\cos\theta(k_x^2 - k_y^2) - 2k_xk_y\sin\theta]\}\sigma_z,\end{aligned} \tag{5}$$

where we have defined $a = \frac{eE_o}{\hbar\omega}$. Now the time dependent Hamiltonian $\mathcal{H}(t)$ satisfies the following Schrödinger equation with the eigenstate $\Psi(x, y, t)$,

$$\mathcal{H}(t)\Psi(x, y, t) = i\hbar\frac{\partial}{\partial t}\Psi(x, y, t). \tag{6}$$

This equation cannot be solved explicitly for $\Psi(x, y, t)$ for the Hamiltonian $\mathcal{H}(t)$ [Eq. (3)]. But as our Hamiltonian $\mathcal{H}(t)$ is periodic in time, i.e., $\mathcal{H}(t) = \mathcal{H}(t + T)$ for the time period $T = 2\pi/\omega$, it is possible to solve the time dependent Schrödinger equation [Eq. (6)] using the Floquet formalism [3,27]. According to the Floquet theory, we can expand the $\Psi(t)$ as a Fourier series in time,

$$\Psi(x, y, t) = \sum_{m=-\infty}^{m=\infty} e^{-i\epsilon t/\hbar}e^{-im\omega t}u^m(x, y), \tag{7}$$

ϵ is the quasienergy eigenvalue for the time independent eigenstate u^m where $m = 0, \pm1, \pm2, \ldots$ is an integer. By substituting $\Psi(t)$ into Eq. (6) and after using the orthogonal properties of function $e^{-im\omega t}$, we get the following equation:

$$\begin{aligned}&\mathcal{H}_o\delta_{n,n}u^n + \left\{\frac{a\hbar v_{xy}}{2}(\sin\theta\sigma_x - \cos\theta\sigma_y) + \lambda_h\left[\frac{3a^3}{8}\cos 3\theta + \frac{3a}{2}\left[\cos\theta(k_x^2 - k_y^2) - 2k_xk_y\sin\theta\right]\right]\sigma_z\right\}(u^{1+n} + u^{n-1}) \\ &+ \frac{3\lambda_h a^2(\cos 2\theta k_x - \sin 2\theta k_y)}{4}\sigma_z\,(2u^n + u^{2+n} + u^{n-2}) + \lambda_h\frac{a^3}{8}\cos 3\theta\,\sigma_z\,(u^{3+n} + u^{-(3-n)}) = (\epsilon + n\omega\hbar)\,\delta_{n,n}\,u^n.\end{aligned} \tag{8}$$

Here, in this work, we have considered the electromagnetic irradiation of the topological insulator surface in the off-resonant regime, i.e., the photon energy of the electromagnetic radiation is greater than the bandwidth of the topological insulator. In the off-resonant regime the electron transition between different energy bands cannot occur due to electromagnetic irradiation of the topological insulator surface (see Refs. [27,28] for a detailed explanation). The Dirac electron states and its transport properties in the off-resonant irradiated topological insulator surface are mainly affected by the modification of the energy band structure induced by the second order virtual photon process [27,28], which consists of the process of photon absorption (emission) followed by the photon emission (absorption) by the electron. This is in contrast to the on-resonant regime, in which the photon energy of electromagnetic radiation [27,28] is smaller than the bandwidth of the topological insulator, which consequently induces inter- and intraband electron transition due to the real photon absorption/emission process and leads to hot carrier transport induced by nonequilibrium distribution of charge carriers in the conduction and valence band [28].

So for the irradiation in the off-resonant regime we have the condition $\frac{eE_o v_{xy}}{\omega} << \hbar\omega$, for this it is appropriate to restrict the value of n up to $n = 0, 1, -1$ [13,14,29]. Hence, under the assumption $eE_o v_{xy} << \hbar\omega^2$, we can ignore the u^n having $n > 1$ in Eq. (8), which leads to the three matrix equations in u^0, u^1, and u^{-1}. These three equations can be further reduced to get the following effective static Hamiltonian for the off-resonant irradiation of topological insulator:

$$\mathcal{H}_{\text{eff}} = \hbar v_{xy}(\sigma_x k_y - \sigma_y k_x) + \lambda_h(k_x^3 - 3k_y^2 k_x)\sigma_z + \Delta\sigma_z + \frac{3\lambda_h a^2}{2}(\cos 2\theta k_x - \sin 2\theta k_y)\sigma_z, \tag{9}$$

which satisfies the Schrödinger equation given by

$$\mathcal{H}_{\text{eff}}\,u^0 = \epsilon\,u^0, \tag{10}$$

where the u^0 is an eigenstate of the Hamiltonian $\mathcal{H}_{\text{eff}}$. It can be seen that Eq. (10) is an easily solvable time independent Schrödinger equation which effectively determines the solution for the time dependent problem represented by Eq. (6). Note that the time independent effective Hamiltonian ($\mathcal{H}_{\text{eff}}$) of Eq. (9) differs from the static surface Hamiltonian $\mathcal{H}_0$ [Eq. (2)] only by the last term in which the hexagonal warping parameter λ_h couples the Dirac surface states to the electromagnetic radiation through the electric field amplitude parameter $a = \frac{eE_o}{\hbar\omega}$. This coupling goes away in the absence of hexagonal warping of the Fermi surface (i.e., $\lambda_h = 0$ or for the low energy Dirac electron). This is in contrast to the off-resonant circular polarized electromagnetic irradiation of the topological insulator surface where the Dirac states also couples with radiation in the absence of hexagonal warping by generating a time reversal breaking mass term in the effective static Hamiltonian. In Refs. [13,14] this was studied in graphene and the topological insulator for the low energy Dirac electron (i.e., $\lambda_h = 0$). In addition to this, the Hamiltonian $\mathcal{H}_{\text{eff}}$ for the linearly polarized radiation is asymmetric under the transformation $\theta \to -\theta$ of the polarization angle but symmetric under the transformation $\theta \to \theta + \pi$. We find the eigenstates u^0 of the time independent effective Hamiltonian $\mathcal{H}_{\text{eff}}$ from Eq. (10) to be

$$u^0(k_x, k_y, s) = \mathcal{N}\begin{bmatrix}\frac{\hbar v_{xy}(k_y + ik_x)}{[\epsilon_s - M(k_x, k_y, \theta)]}\\ 1\end{bmatrix}, \tag{11}$$

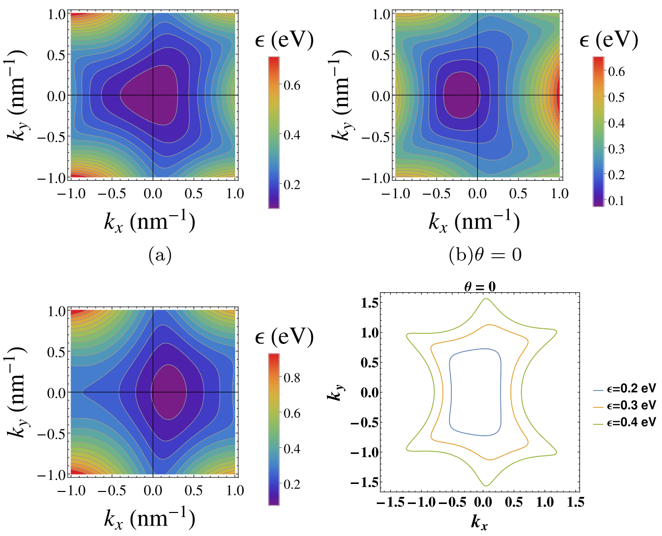

(a) (b)$\theta = 0$

(c)$\theta = \pi/2$ (d)

FIG. 2. The figures show the contour plots for the conduction band quasienergy ϵ in momentum space, (a) in the absence of electromagnetic field, (b) and (c) in the presence of electromagnetic field ($a \neq 0$) for different polarization angle θ, and (d) energy contours in the momentum space for $\theta = 0$ for different energies ϵ.

where $M(k_x, k_y, \theta) = \lambda_h(k_x^3 - 3k_y^2 k_x) + \Delta + \frac{3\lambda_h a^2}{2}(\cos 2\theta k_x - \sin 2\theta k_y)$ and $\mathcal{N}$ is the normalization constant, given by

$$\mathcal{N} = \left[1 + \frac{\hbar^2 v_{xy}^2 \left(k_x^2 + k_y^2\right)}{(\epsilon_s - M)^2}\right]^{-1/2}. \tag{12}$$

The energy eigenvalue ϵ_s for the Hamiltonian $\mathcal{H}_{\text{eff}}$ is

$$\epsilon_s = s\Big[\hbar^2 v_{xy}^2\left(k_x^2 + k_y^2\right) + \big[\lambda_h\left(k_x^3 - 3k_y^2 k_x\right) + \Delta + \frac{3\lambda_h a^2}{2}(\cos 2\theta k_x - \sin 2\theta k_y)\big]^2\Big]^{1/2}, \tag{13}$$

where the $s = \pm$ denotes the conduction and valence band of the energy spectrum. Before we proceed further, note that for the calculations of the physical quantities in this paper, we will use the photon energy in the off-resonant regime with value $\hbar\omega = 8$ eV [28], which corresponds to a frequency of radiation $\nu = 1.93 \times 10^{15}$ Hz. So that in the off-resonant regime, i.e., $\frac{eE_o v_{xy}}{\omega} << \hbar\omega$, we will assume $\frac{eE_o v_{xy}}{\omega}$ in the range 0.1 to 0.9 eV which corresponds to the value of the electric field parameter $a = eE_o/\hbar\omega$ in the range 0.39 to 3.54 nm^{-1}. Other parameters which we use for calculations are $\lambda_h = 0.250$ eV nm^3, $\hbar v_{xy} = 0.255$ eV nm, and $\Delta = 0.07$ eV. The contour plot for the conduction energy band is plotted in the momentum space in the presence and absence of radiation in Fig. 2, respectively. The comparison of Fig. 2(a) with Figs. 2(b) and 2(c) reveals that the linearly polarized electromagnetic irradiation drastically deforms the Fermi energy contours in addition to the deformation produced by the hexagonal warping in the absence of radiation [Fig. 2(a)].

B. Spin texture of the surface states

The spin texture of the surface states is the vector field in momentum space of expectation values of the spin with orientations as calculated below. Here we find the spin orientation in the spin texture of the surface states u^0 [Eq. (11)], induced on the surface of the topological insulator illuminated with linearly polarized electromagnetic radiation, is as follows:

$$\begin{aligned} \vec{S} &= \frac{\hbar}{2}\langle u^0|\vec{\sigma}|u^0\rangle \\ &= \frac{\hbar}{2}[\langle\sigma_x\rangle\hat{x} + \langle\sigma_y\rangle\hat{y} + \langle\sigma_z\rangle\hat{z}], \end{aligned} \tag{14}$$

where for the eigenstates u^0 [Eq. (11)] the $\langle\sigma_x\rangle$, $\langle\sigma_y\rangle$, and $\langle\sigma_z\rangle$ are given by

$$\langle\sigma_x\rangle = \frac{2\mathcal{N}^2\hbar v_{xy} k_y}{[\epsilon_s - M(k_x, k_y, \theta)]}, \tag{15a}$$

$$\langle\sigma_y\rangle = -\frac{2\mathcal{N}^2\hbar v_{xy} k_x}{[\epsilon_s - M(k_x, k_y, \theta)]}, \tag{15b}$$

$$\langle\sigma_z\rangle = \mathcal{N}^2\left\{\frac{\hbar^2 v_{xy}^2\left(k_x^2 + k_y^2\right)}{[\epsilon_s - M(k_x, k_y, \theta)]^2} - 1\right\}. \tag{15c}$$

We plot the spin texture in Fig. 3 for the surface states of the topological insulator in the conduction band using Eqs. (15a)–(15c) in momentum space. In the absence of band gap and hexagonal warping, the spin texture of Fig. 3(a) shows that at low energy there is only in-plane spin components present in the surface states and the states are spin-momentum locked. This is intrinsically related to the terms of the surface state Hamiltonian $\mathcal{H}_{\text{eff}}$ [Eq. (9)], which for $\Delta = 0$ and $\lambda_h = 0$, contains only σ_x and σ_y Pauli matrices (corresponding to S_x and S_y in-plane components of spin). But for $\Delta \neq 0$ (nonzero band gap) and $\lambda_h \neq 0$ (nonzero hexagonal warping) the Hamiltonian also includes a term consist of a Pauli matrix corresponding to the z-component of spin, i.e., σ_z. As a result, for both $\Delta \neq 0$ and the nonzero hexagonal warping (for $\lambda_h \neq 0$), the spin texture exhibits z component of spin in addition to in-plane components, as shown in Figs. 3(b) and 3(e) (note that $s_z/\hbar$ is nonzero). Furthermore, hexagonal warping of the Fermi surface leads to a C_3 rotation symmetric anisotropic spin texture [see Figs. 3(b) and 3(e)] of surface states, which is otherwise isotropic in the absence of hexagonal warping [see Fig. 3(a)]. On the other hand, we find that the presence of the linearly polarized electromagnetic irradiation [see Figs. 3(c), 3(d), 3(f), and 3(g)], breaks the C_3 rotation symmetry of the spin texture of the surface states in momentum space. Note that C_3 rotation symmetry [Figs. 3(b) and 3(e)] and broken C_3 symmetry [Figs. 3(c), 3(d), 3(f), and 3(g)] possessed by spin texture, are inherited from the C_3 symmetric k-cubic hexagonal warping term and C_3 symmetry breaking radiation induced term of the Hamiltonian [Eq. (9)], respectively. Hence, the linear polarized irradiation provides a possibility of tuning the spin texture by varying the amplitude and polarization angle θ. It can be seen from Figs. 4(a)–4(d) that the average spin components [24] varies periodically but nonsinusoidally with polarization angle θ. Whereas if we vary the amplitude parameter a, we find that S_x monotonically increases and saturates, S_y first increases and then decays down to zero,

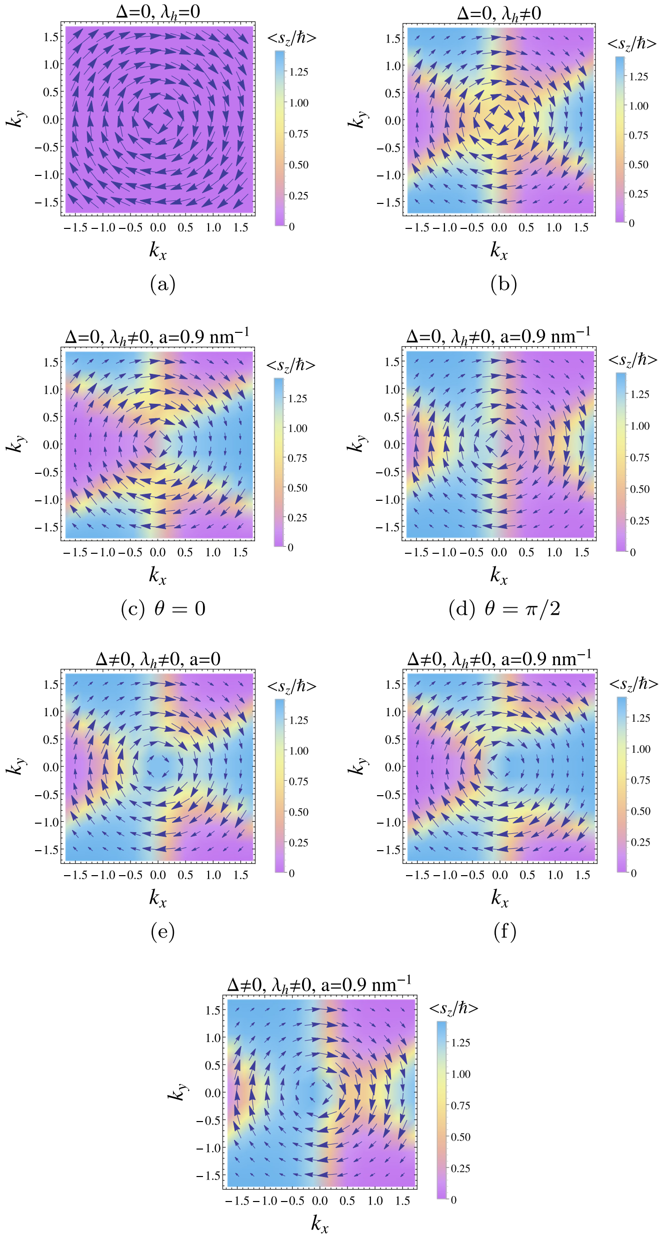

(a) (b)

(c) $\theta = 0$ (d) $\theta = \pi/2$

(e) (f)

(g) $\theta = 0$

FIG. 3. The figures show the spin texture of the surface states of the topological insulator in momentum space for zero band gap ($\Delta = 0$), (a) in the absence of hexagonal warping and the electromagnetic field ($\lambda = 0, a = 0$), (b) in the presence of hexagonal warping and the absence of the electromagnetic field ($\lambda \neq 0, a = 0$), and (c) and (d) in the presence of hexagonal warping and electromagnetic field ($\lambda \neq 0, a \neq 0$) for different polarization angle $\theta = 0, \pi/2$. The spin texture for the nonzero band gap case are shown in (e) for ($\lambda \neq 0, a = 0$) and (f) and (g) for ($\lambda \neq 0, a \neq 0$).

and S_z monotonically decreases to negligible values (near zero) as we increase the amplitude of the radiation. We will see, in the next sections, that both deformation produced in the Fermi surface and the modification of the spin texture by the linearly polarized radiation has a major contribution in determining the effect of irradiation on the thermoelectric properties of the topological insulator surface. Furthermore, we will calculate the Berry curvature, Berry phase, and the anomalous Hall conductivity associated with Floquet-Dirac surface states induced by the linearly polarized radiation.

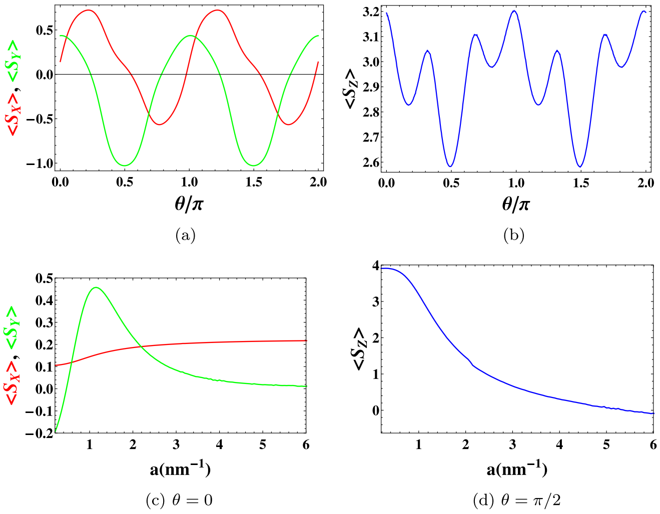

(a) (b)

(c) $\theta = 0$ (d) $\theta = \pi/2$

FIG. 4. The figures shows the average spin components $\langle S_x \rangle$, $\langle S_y \rangle$, and $\langle S_z \rangle$ as a function of (a) and (b) polarization angle θ and (c) and (d) the radiation amplitude parameter (a).

III. BERRY CURVATURE, BERRY PHASE, AND ANOMALOUS HALL CONDUCTIVITY

A. Berry curvature

The nonzero Berry curvature associated with the conduction and valence energy band in a crystalline materials leads to the anomalous group velocity of an electron, anomalous orbital band magnetization, and anomalous thermoelectric transport [18,30]. We have calculated the Berry curvature ($\vec{\Omega}_s$) using the eigenstates [Eq. (11)] of the Hamiltonian $\mathcal{H}_{\text{eff}}$ for the conduction and valence band, which is given below:

$$\vec{\Omega}_s = i\vec{\nabla}_k \times \langle u^o(k_x, k_y, s)|\vec{\nabla}_k|u^o(k_x, k_y, s)\rangle \quad (16)$$

$$= -\frac{s\,\hbar^2 v_{xy}^2\left[\Delta - 2\lambda_h\left(k_x^3 - 3k_y^2 k_x\right)\right]}{2\left\{\hbar^2 v_{xy}^2\left(k_x^2 + k_y^2\right) + [M(k_x, k_y, \theta)]^2\right\}^{3/2}}\hat{z}, \quad (17)$$

where $s = +\,(-)$ denotes the conduction (valence) band and Eq. (17) reflects that the Berry curvature for the valence band is just opposite in sign to the Berry curvature for the conduction band, i.e., $\vec{\Omega}_- = -\vec{\Omega}_+$. Furthermore, it can be seen from Eq. (17) that the Berry curvature is dependent upon the polarization angle θ of the linearly polarized electromagnetic radiation with which the topological insulator surface is irradiated. Equation (17) also shows that the Berry curvature is θ dependent only in the presence of the hexagonal warping effect in the band structure, because for the $\lambda_h = 0$ the Berry curvature [Eq. (17)] becomes

$$\vec{\Omega}_s = -\frac{s\,\hbar^2 v_{xy}^2 \Delta}{2\left\{\hbar^2 v_{xy}^2\left(k_x^2 + k_y^2\right) + \Delta^2\right\}^{3/2}}\hat{z}. \quad (18)$$

Note this is just the Berry curvature without the hexagonal warping and the dependence of the angle θ. In the absence of linearly polarized light, i.e., $a = 0$, our expression of Berry curvature [Eq. (17)] becomes

$$\vec{\Omega}_s = -\frac{s\,\hbar^2 v_{xy}^2\left[\Delta - 2\lambda_h\left(k_x^3 - 3k_y^2 k_x\right)\right]}{2\left\{\hbar^2 v_{xy}^2\left(k_x^2 + k_y^2\right) + \left[\lambda_h\left(k_x^3 - 3k_y^2 k_x\right) + \Delta\right]^2\right\}^{3/2}}\hat{z}, \tag{19}$$

which is the same as the Berry curvature of the topological insulator calculated in Ref. [24] in the presence of the hexagonal warping effect.

Furthermore, as we make $k_x \rightarrow 0$ and $k_y \rightarrow 0$ in Eq. (17), the Berry curvature becomes $\vec{\Omega}_s(k_x, k_y, \theta) = -\frac{s\,\hbar^2 v_{xy}^2}{\Delta^2}\hat{z}$, this means the Berry curvature is inversely proportional to the square of the band gap Δ. As a result, when $\Delta \rightarrow 0$, the Berry curvature becomes singular at the center of the Brillouin zone, i.e., at $(k_x, k_y) = 0$, which otherwise is nonsingular if $\Delta \neq 0$. The above discussed singularity of the Berry curvature reflects the presence of a sink or source (a topological charge [31,32]) at the origin of parameter space defined by Δ, k_x, k_y, i.e., at $(k_x, k_y, \Delta) = (0, 0, 0)$, which generates this Berry curvature. This, just like the singularity of the electrostatic field in real space, implies the presence of charge at the point of singularity. The topological charge associated with this singularity is calculated via the flux of Berry curvature over the closed surface enclosing this singularity in the parameter space divided by factor of 2π, which is nothing but a topological invariant that does not depend upon the shape of the considered closed surface, and is hence topological in nature [31]. Furthermore, the Berry curvature of Eq. (17) can be written as $-s\,\hbar^2 v_{xy}^2[\Delta - 2\lambda_h(k_x^3 - 3k_y^2 k_x)]/2\epsilon_s^3\hat{z}$, which reflects that the singularity of the Berry curvature occurs at $\epsilon_s = 0$. Thus the singularity of the Berry curvature also implies the presence of a point of degeneracy in the Brillouin zone, which can be seen from Eq. (13) where for $\Delta = 0$ the valence and conduction band touches at $(k_x, k_y) = (0, 0)$.

We plotted the contour plots of the Berry curvature in momentum space in Fig. 5 for the cases $\Delta = 0$ and $\Delta \neq 0$ in the conduction band. The singularity of the Berry curvature can be seen clearly at $k_x, ky = 0$ for $\Delta = 0$ in Figs. 5(a)–5(c), which gets removed as we make $\Delta \neq 0$ [see Figs. 5(d)–5(f)]. The Berry curvature in the absence of band gap and radiation but in the presence of hexagonal warping (i.e., $\Delta = 0$ and $a = 0$) exhibits threefold rotation symmetry in the momentum space [as shown in Fig. 5(a)] and switches its value from positive to negative alternatively at the angle of $\pi/6$. This behavior of the Berry curvature in the momentum space is due to the hexagonal nature of the Fermi surface of the energy band induced by the presence of a threefold rotation symmetric k-cubic hexagonal warping term in the Hamiltonian $\mathcal{H}_{\text{eff}}$. This threefold symmetry of Berry curvature in the momentum space breaks as soon as we turn on the electromagnetic radiation, i.e., $a \neq 0$ [see Figs. 5(b) and 5(c)]. Furthermore, the presence of the electromagnetic radiation also makes the Berry curvature polarization angle θ dependent, which can be seen from Figs. 5(b) and 5(c). The Berry curvature has asymmetric contours in momentum space and the positions of the asymmetry arising in the Berry curvature in momentum space changes with the change in the angle θ of polarization.

The presence of a gap, i.e., $\Delta \neq 0$, reshapes the Berry curvature contours in the absence of electromagnetic radiation ($a = 0$) [see Fig. 5(d)] as compared to the contours in the absence of a gap [Fig. 5(a)], but the threefold symmetry can still be seen in the Berry curvature. For the case $\Delta \neq 0$, the presence of electromagnetic radiation ($a \neq 0$) leads to the broken threefold symmetry of the Berry curvature and its polarization angle θ dependence, as can be seen from Figs. 5(e) and 5(f). For $\Delta \neq 0$, the presence of radiation also shifts the position of the Berry curvature peak from $k_x, k_y = 0$ [Figs. 5(d)–5(f)]. Which is in contrast to the $\Delta = 0$ case in which the Berry curvature peak remains at $k_x, k_y = 0$ even in the presence of the radiation [see Figs. 5(a)–5(c)].

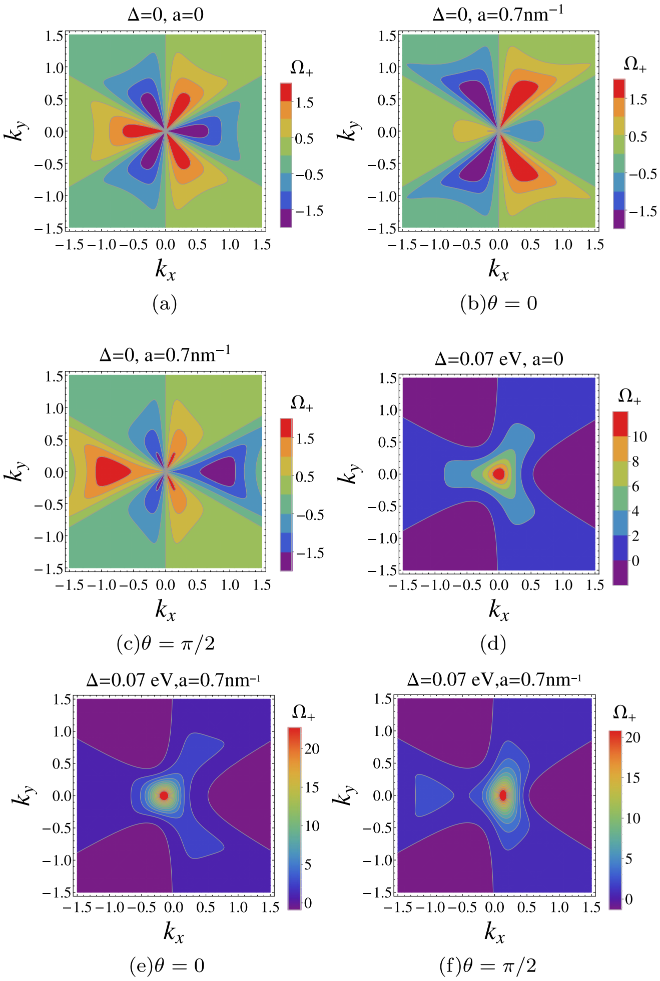

(a) (b)$\theta = 0$

(c)$\theta = \pi/2$ (d)

(e)$\theta = 0$ (f)$\theta = \pi/2$

FIG. 5. (a)–(c) The contour plots of the Berry curvature in momentum space for the zero band gap ($\Delta = 0$), (a) in the absence of electromagnetic field, and (b) and (c) in the presence of electromagnetic field ($a \neq 0$) for different polarization angle θ. The Berry curvature for the nonzero band gap ($\Delta \neq 0$) is shown in (d) in the absence of the electromagnetic field, and (e) and (f) in the presence of the electromagnetic field.

B. Berry phase

When a system adiabatically evolves in time with the state moving slowly over a closed path in parameter space, the state gains a gauge invariant phase called the Berry phase [31,33], which is the flux of Berry curvature on the surface enclosed by that closed path in parameter space. The Berry curvature dependency on the polarization angle θ of linearly polarized electromagnetic radiation, as calculated in the previous section, also causes the Berry phase of the Floquet-Dirac states in the irradiated topological insulator to depend upon the angle θ. The Berry phase can be calculated by the surface integral of the Berry curvature in the first Brillouin zone of the topological insulator [31]. For the Fermi energy in the conduction band, we calculated the Berry phase over the closed path $\mathcal{C}$, represented by a deformed contour in BZ, as shown in Figs. 2(b) and 2(c). The Berry phase is given by [31,33]

$$\Lambda_B = \iint_{\mathcal{S}} \Omega_+(k_x, k_y, \theta)\, dk_x dk_y, \tag{20}$$

where $\mathcal{S}$ is the area in the positive $\hat{z}$ direction enclosed by the closed curve $\mathcal{C}$ in the Brillouin zone. By putting $k_x = k\cos\alpha$ and $k_y = k\sin\alpha$ in the Berry curvature Ω_+ of Eq. (17) and then using that modified Berry curvature in Eq. (20) we get the following expression of the Berry phase:

$$\begin{aligned}\Lambda_B(\theta, a) &= -\int_{\alpha=0}^{2\pi}\int_{k=0}^{k_f(\alpha)} \frac{\hbar^2 \nu_{xy}^2[\Delta - 2\lambda_h k^3\cos 3\alpha]\, k\, dk\, d\alpha}{2\left\{\hbar^2\nu_{xy}^2 k^2 + \left[\lambda_h k^3 \cos 3\alpha + \Delta + \frac{3\lambda_h a^2 k}{2}\cos(2\theta+\alpha)\right]^2\right\}^{3/2}} \\ &= -\pi + \int_{\alpha=0}^{2\pi} \frac{\left[\Delta + \lambda_h k_f^3(\alpha)\cos 3\alpha + (3/2)\lambda_h a^2 k_f \cos(2\theta+\alpha)\right]}{2\left\{\hbar^2\nu_{xy}^2 k_f^2(\alpha) + \left[\lambda_h k_f^3(\alpha)\cos 3\alpha + \Delta + \frac{3\lambda_h a^2 k_f(\alpha)}{2}\cos(2\theta+\alpha)\right]^2\right\}^{1/2}}\, d\alpha.\end{aligned} \tag{21}$$

In Eq. (21), $k_f(\alpha)$ is the Fermi wave vector and is the positive real root of the following polynomial equation [found by using Eq. (13)]:

$$\begin{aligned}&\lambda_h^2 k_f^6\cos^2 3\alpha + 3\lambda_h^2 a^2 k_f^4 \cos 3\alpha\cos(2\theta+\alpha) + 2\Delta\lambda_h k_f^3\cos 3\alpha + \left[\hbar^2\nu_{xy}^2 + \frac{9\lambda_h^2 a^4}{4}\cos^2(2\theta+\alpha)\right]k_f^2 \\ &+3\lambda_h\Delta\, a^2\cos(2\theta+\alpha)\, k_f + \Delta^2 = \epsilon_f^2,\end{aligned} \tag{22}$$

where ϵ_f is the Fermi energy. By solving Eq. (21) numerically we calculated the Berry phase as a function of the polarization angle θ, which we plotted in Fig. 6(a). Figure 6(a) shows that the Berry phase sinusoidally varies with polarization angle θ of the electromagnetic radiation. It can be noted from Fig. 6(a) that there are exactly six maxima and six minima in the plot of the Berry phase. This is a consequence of the anisotropic coupling of off-resonant electromagnetic radiation with the momentum of the Dirac surface states, because there are exactly six points in the hexagonally warped Fermi surface where the length of Fermi momentum is a maximum and exactly six points where it is a minimum [see contours in Figs. 2(b) and 2(c)]. Interestingly, the Berry phase calculated in Eq. (21) can be resolved in the following form, i.e.,

$$\Lambda_B = -\pi + \Delta\, P + \lambda_h\, Q + \lambda_h\, a^2\, R. \tag{23}$$

Where P, Q, and R are the functions of parameters λ_h, a, ϵ_f, θ, obtained after solving the integrals of Eq. (21).

This expression reflects a important relation between the Berry phase and the spin texture associated with the surface states of the topological insulator. For the case when there is no band gap and hexagonal warping, i.e., $\Delta = 0$ and $\lambda_h = 0$, the Berry phase is given by $\Lambda_B = -\pi$. Physically, the spin rotation or parallel transport of a spinor of a fermion on a closed path by a 2π angle corresponds to the Berry phase of value $\pm\pi$. In the topological insulator, this $|\pi|$ value of Berry phase corresponds to the occurrence of helical surface states exhibiting in-plane spin-momentum locked spin texture either in clockwise or anticlockwise direction [34–36] [as shown in Fig. 3(a)]. In Fig. 3(a) the spin actually shows rotation by the 2π angle in the momentum space and hence corresponds to π Berry phase. The usual metals have states having spin texture in both clockwise and anticlockwise direction and hence correspond to Berry phase of value zero. On having band gap in the energy spectrum in the absence of hexagonal warping, i.e., $\Delta \neq 0$ and $\lambda_h = 0$, the Berry phase value becomes $\Lambda_B = -\pi(1 - \Delta/\epsilon_f)$ [obtained by solving Eq. (21), for which we get $P = \pi/\epsilon_f$] [24]. As already explained in Sec. II B, Δ leads to the z component of spin in the spin texture, hence the occurrence of the out-of-plane spin component in the spin texture which changes the value of Berry phase [24]. Furthermore, the inclusion of the hexagonal warping ($\lambda_h \neq 0$) and the radiation ($a \neq 0$) individually alter the z component of spin [see Figs. 3(b)– 3(d) and explanation in Sec. II B], results in a modification of the Berry phase, as reflected by Eq. (23). The dependence of Berry phase on the z component of spin can be more clearly understood by the variation of Berry phase with the change in the amplitude parameter a of the radiation, which is plotted in Fig. 6(b). The Berry phase strongly depends upon the amplitude of the electric field of the linearly polarized electromagnetic radiation. Figure 6(b) shows that the Berry phase magnitude ($|\Lambda_B|$) increases with the increase in the value of the amplitude of the electric field of the electromagnetic radiation. The Berry phase saturates to the value $|\pi|$ at high values of the electric field amplitude and has a value less than $|\pi|$ at low amplitudes of the electric field. It can be seen from Eq. (21) that the Berry phase is a sum of a constant factor of $-\pi$ and an electric field amplitude parameter a dependent term. This radiation dependent term effectively reduces as we increase the electric field amplitude leaving behind the value close to $-\pi$ for high electric fields. This happens because the average magnitude of the z component of spin of the surface states decreases as we increase the amplitude parameter a [see Fig. 4(d)], and hence the contribution of the extra terms in Eq. (23)

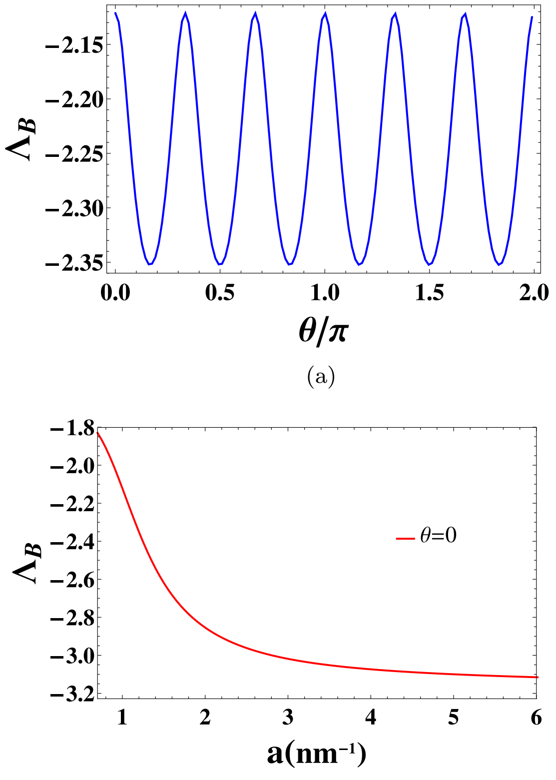

(a)

(b)$\theta = 0$

FIG. 6. The figures shows variation in the Berry phase Λ_B with (a) polarization angle θ and (b) electric field amplitude parameter $a = eE_o/\hbar\omega$.

other than $-\pi$ (i.e., Δ, λ_h, and a dependent terms, which generates S_z component in spin texture) to the Berry phase effectively reduces for high a and Berry phase approaches the value close to $-\pi$. This strengthens the fact that Berry phase and the spin texture are related to each other. The Berry phase can also be calculated for the case in which the angle of polarization θ is varied adiabatically. For this, the Berry phase is given by the following equation: $\Lambda_B = \oint_0^{2\pi} A_B(\theta)d\theta$, where $A_B(\theta)$ is the Berry connection given by $A_B(\theta) = i\langle u^o(k_x, k_y, \theta)|\frac{\partial}{\partial\theta}|u^o(k_x, k_y, \theta)\rangle$. We calculated the Berry connection using the states of Eq. (11), which we find comes out to be $A_B(\theta) = 0$. So, for cyclic adiabatic variation of polarization angle θ, the Berry phase is $\Lambda_B = 0$. This zero Berry phase is a consequence of the absence of degeneracy point in the energy spectrum for any value of θ (i.e., there is no value of θ for which $\epsilon_s = 0$ at finite value of Δ, k_x, k_y).

C. Anomalous Hall conductivity

The nonzero Berry phase results in the occurrence of the anomalous Hall effect in crystalline materials having a nonzero Berry curvature associated with energy bands. In the anomalous Hall effect (AHE), there is a generation of the transverse Hall current in the material by the transport driven by either a mechanical force, like the electric field, or a statistical force, like gradient of chemical potential (μ), i.e., $\vec{\nabla}\mu$. In the case of the electric field, the anomalous Hall effect is generated by the Berry curvature dependent anomalous term present in the group velocity of the Bloch electron [18]. Whereas, in the case of the chemical potential gradient, AHE occurs due to the Berry curvature induced correction in the orbital magnetization of the Bloch electrons [18]. In both cases the Berry curvature plays an important role in determining the anomalous Hall current.

Now, as we show in Secs. III A and III B, the linearly polarized electromagnetic irradiation of the topological insulator surface leads to a radiation parameter (amplitude and polarization) dependent Berry curvature and Berry phase associated with the Floquet-Dirac surface states. In this section we analyze the effect of linearly polarized irradiation of TI surface on the anomalous Hall conductivity associated with anomalous Hall current, in the presence of nonzero hexagonal warping of a Fermi surface. Consider on the topological insulator surface that a transverse Hall current $j_{e,x}$ is generated via AHE in the presence of electric field E_y in the y direction, which is given by [18]

$$j_{e,x} = \sigma_{xy}E_y, \tag{24}$$

where the σ_{xy} is the transverse Hall conductivity given by the integral of Berry curvature over the momentum space multiplied by the $e^2/\hbar$ [18],

$$\sigma_{xy} = \frac{e^2}{\hbar}\int \Omega(\vec{k})f_{\text{eq}}\frac{d^2\vec{k}}{(2\pi)^2}, \tag{25}$$

where $\Omega(\vec{k})$ is the Berry curvature and $f_{\text{eq}} = 1/(1 + e^{(\epsilon_s-\mu)/k_BT})$ is the equilibrium Fermi-Dirac distribution function. For the energy ϵ_s [Eq. (13)] and the Berry curvature $\vec{\Omega}_s$ [Eq. (17)], we can write the above equation in the following form:

$$\sigma_{xy}(\theta, a, \mu, T) = \frac{e^2}{2\pi h}\sum_{s=\pm}\iint f_{\text{eq}}\,\Omega_s(\theta, \alpha, k)k\,dk d\alpha. \tag{26}$$

In Eq. (26) the sum is over the filled energy bands defined by $s = +\,(-)$ for the conduction (valence) energy band. To illustrate the behavior of the transverse Hall conductivity analytically, we determine the σ_{xy} in the low temperature regime. For low temperature, i.e., $T \to 0$, Eq. (26) reduces to

$$\sigma_{xy}(\theta, a, \mu, T) = \frac{e^2}{2\pi h}\sum_{s=\pm}\iint \Omega_s(\theta, \alpha, k)\Theta(\mu - \epsilon_s)k\,dk d\alpha, \tag{27}$$

where $\Theta(\mu - \epsilon_s)$ is the Heaviside step function. Equation (27) can be solved analytically for the $\lambda = 0$ case only, i.e., without hexagonal warping of the Fermi surface. So for the Berry curvature for $\lambda = 0$ [Eq. (18)], we find the Hall conductivity to be $\sigma_{xy} = \frac{e^2}{h}\frac{\Delta}{\mu}$ for μ in conduction and valence band. This implies that the σ_{xy} for μ inside the conduction and valence band is inversely proportional to the chemical potential. This means σ_{xy} is maximum at the bottom of the conduction band and the top of the valence band (i.e., for $|\mu| = |\Delta|$) and it decreases as we move deeper into the conduction and valence band, i.e., for $\mu \gg \Delta$ or $\mu \ll -\Delta$. For μ inside the band gap, i.e., $-\Delta < \mu < \Delta$, we find σ_{xy} is constant and is given by $\sigma_{xy} = e^2/h$. Equation (27) implies the anomalous Hall conductivity at low temperature is the sum of the Berry phase associated with the filled conduction and valence band. At high temperature, the Heaviside step function $\Theta(\mu - \epsilon_s)$ thermally broadens in the region $|\mu - \epsilon_s| < k_B T$. To show the dependence of conductivity σ_{xy} on different model parameters, at finite temperature $T > 0$, we numerically calculated and plotted the σ_{xy} as a function of polarization angle θ, electric field amplitude parameter a, the chemical potential μ, and the temperature T in Figs. 7(a)–7(d).

We find the σ_{xy} shows sinusoidal variation as we change the polarization angle θ, this is a result of the polarization angle dependency of the Berry curvature Ω_s and the Berry phase, on which the conductivity σ_{xy} depends directly. The conductivity σ_{xy} decreases as we increases the amplitude parameter a of the electric field of the radiation (which is the same as the variation in the Berry phase with a). The variation of the σ_{xy} as a function of the chemical potential μ is shown in Fig. 7(c) for the case of zero hexagonal warping (i.e., $\lambda_h = 0$, black dotted curve), nonzero hexagonal warping with out any electromagnetic radiation (i.e., $a = 0$ and $\lambda_h \neq 0$, blue curve), and nonzero hexagonal warping with electromagnetic radiation (i.e., $a \neq 0$ and $\lambda_h \neq 0$, green and red curve for $\theta = 0$ and $\theta = \pi/2$, respectively). Figure 7(c) shows that the Hall conductivity σ_{xy} has a greater value for the case when there is no hexagonal warping (black dotted curve) than the case for which the hexagonal warping is nonzero (blue curve) in both the conduction and valence band, respectively. This change in the Hall conductivity σ_{xy} for $\lambda_h \neq 0$ can be attributed to (i) the anisotropicity induced by the hexagonal warping in the Fermi surface of the energy band structure in the Brillouin zone [see deformed contours in Fig. 2(a)], which is absent for the case of $\lambda_h = 0$ because of the isotropic circular Fermi surface of the energy band structure and (ii) the change in the spin texture of the surface states of the topological insulator induced by the hexagonal warping. The spin of the electron is locked with its momentum on the surface of TI. In the absence of hexagonal warping, the spin texture of surface states shows the presence of only in-plane components of spin in the surface states [see Fig. 3(a)] and is isotropic in momentum space. Whereas, in the presence of hexagonal warping, the spin texture in momentum space becomes threefold rotation symmetric and shows the presence of an out-of-plane spin component in addition to the in-plane components [see Fig. 3(b)]. As the Hall conductivity is determined by the sum of the Berry curvature Ω_s (which intrinsically encodes the spin texture information of the surface states u_α^0) over the states of the valence and conduction bands, it is strongly affected by both the shape of the Fermi surface and the spin texture of surface states. As shown in Fig. 7(c) (black and blue curve) σ_{xy} changes if the hexagonal warping goes from zero to nonzero. In addition to the anisotropy induced by the hexagonal warping, the Fermi surface of the energy band and the spin texture are further modified by the presence of electromagnetic radiation [i.e., for $a \neq 0$ see contours in Figs. 2(b) and 2(c) and for the spin texture see Figs. 3(c) and 3(d)]. The effect of this modification due to electromagnetic radiation can be seen in the variation of Hall conductivity σ_{xy} with μ for $a \neq 0$ and $\lambda_h \neq 0$ [see Fig. 7(c) green and red curves], for which the conductivity σ_{xy} is less than the Hall conductivity for the case of hexagonal warping without electromagnetic radiation (i.e., $a = 0$ and $\lambda_h \neq 0$, blue curve). The effect of the modification of the

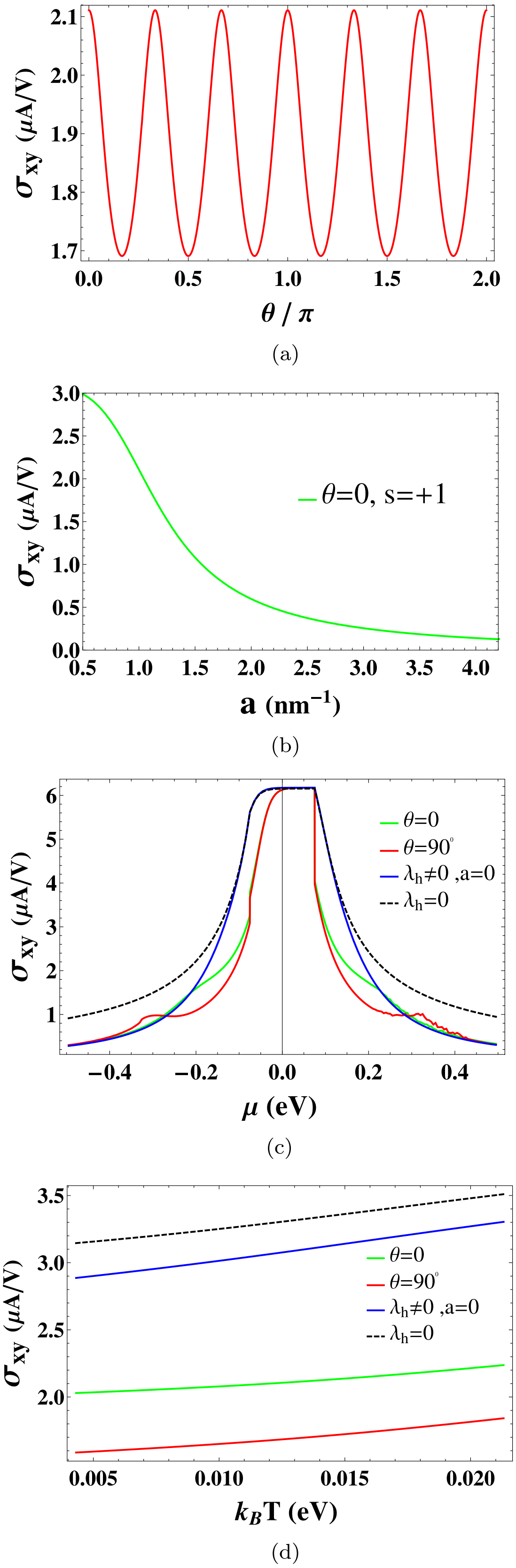

(a)

(b)

(c)

(d)

FIG. 7. The anomalous Hall conductivity σ_{xy} is shown in (a)–(d) as a function of (a) the polarization angle θ, (b) the radiation parameter a, (c) the chemical potential μ, and (d) the temperature.

shape of the Fermi surface and the spin texture by the radiation is more pronouncedly seen in the anomalous thermoelectric conductivities about which we will discuss in Sec. V.

Furthermore, the conductivity σ_{xy} for all the cases decreases to zero as we move deeper into the conduction band or valence band [see Fig. 10(c) for high positive and low negative values of μ]. This is similar to the inverse dependence of the σ_{xy} on μ at low temperature as explained before, i.e., for μ in the conductance and valence band, $\sigma_{xy} = \frac{e^2}{h}\frac{\Delta}{\mu}$. The only difference is that here the temperature is greater than zero and due to thermal broadening of the step function $\Theta(\mu - \epsilon_s)$ of Eq. (27), the value of the σ_{xy} has decreased as compared to the value at $T = 0$ [e.g., for μ inside the band gap, at $T = 0$, we have $\sigma_{xy} = e^2/h = 38.7\ \mu\text{A/V}$ but for $T > 0$, the $\sigma_{xy} < e^2/h$, see Fig. 7(c)].

IV. ORBITAL MAGNETIC MOMENT AND MAGNETIZATION

The Bloch electron in a periodic crystal exhibits orbital magnetic moment in the presence of electromagnetic field due to the self-rotation of the Bloch electron wave packet in the semiclassical picture [18,30]. For the eigenstates u^o, the orbital magnetic moment is defined by the following expression [30,37]:

$$\vec{m}_z(k_x, k_y, \theta) = -i\frac{e}{2\hbar}\langle\vec{\nabla}_k u^o| \times (H_{\text{eff}} - \epsilon_s)|\vec{\nabla}_k u^o\rangle. \tag{28}$$

By using Eq. (11), we find the orbital magnetic moment as a function of the polarization angle θ and wave vector (k_x, k_y) in the following form:

$$\vec{m}_z(k_x, k_y, \theta) = \frac{(-e/2\hbar)\,\hbar^2 v_{xy}^2\left[\Delta - 2\lambda_h\left(k_x^3 - 3k_y^2 k_x\right)\right]}{\left\{\hbar^2 v_{xy}^2\left(k_x^2 + k_y^2\right) + [M(k_x, k_y, \theta)]^2\right\}}\hat{z}. \tag{29}$$

Note that the orbital magnetic moment of Eq. (29) exhibits the same sign in both the conduction and valence band which is attributed to the particle-hole symmetry present in the system. Similar to the Berry curvature, the orbital magnetic moment of the Bloch electron also depends upon the polarization angle θ, only in the presence of nonzero hexagonal warping of the Fermi surface. As can be seen from Eq. (29) for $\lambda_h = 0$, the magnetic moment becomes

$$\vec{m}_z(k_x, k_y, \theta) = \frac{(-e/2\hbar)\,\hbar^2 v_{xy}^2 \Delta}{\left[\hbar^2 v_{xy}^2\left(k_x^2 + k_y^2\right) + \Delta^2\right]}\hat{z}, \tag{30}$$

which is independent of the polarization angle θ, and is the same expression as the orbital magnetic moment found in Ref. [24] in the absence of the hexagonal warping effect.

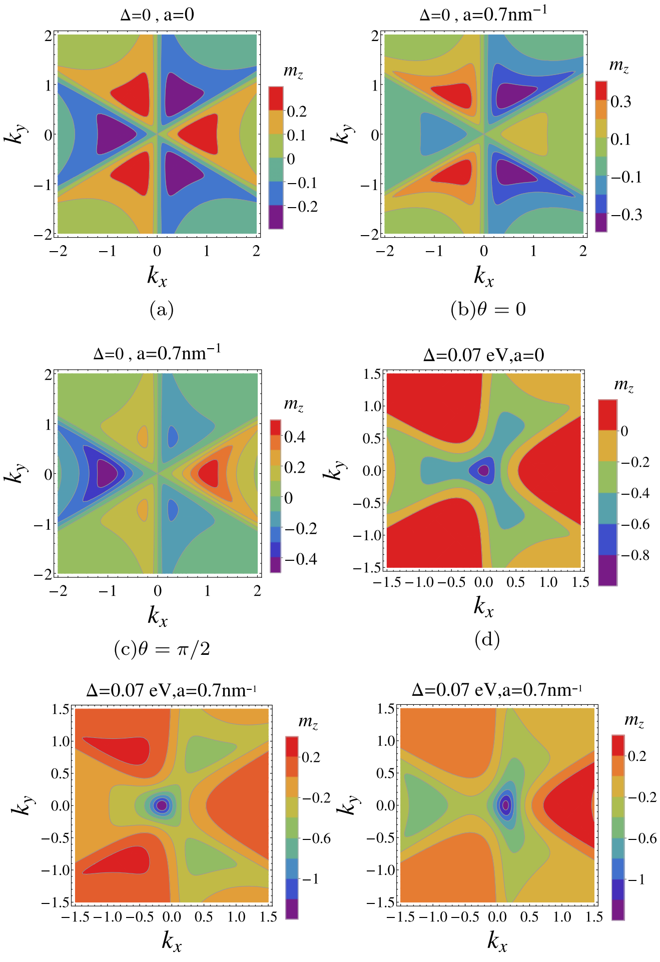

(a) (b)$\theta = 0$

(c)$\theta = \pi/2$ (d)

(e)$\theta = 0$ (f)$\theta = \pi/2$

FIG. 8. The contour plots of orbital magnetic moment m_z in momentum space for zero band gap ($\Delta = 0$) are shown in (a) in the absence of the electromagnetic field, and (b) and (c) in the presence of the electromagnetic field ($a \neq 0$) for different polarization angle θ. For nonzero band gap ($\Delta \neq 0$) contour plots are shown in (d) in the absence of electromagnetic field, and (e) and (f) in the presence of electromagnetic field.

Also, for the $k_x, k_y = (0, 0)$, Eq. (29) shows that the magnetic moment is inversely proportional to the band gap Δ, i.e., $m_z = \frac{(-e)\,\hbar v_{xy}^2}{2\Delta}$. This is different from the Berry curvature, which at $k_x, k_y = 0$, varies as $\Omega_s \propto 1/\Delta^2$. Thus, the orbital magnetic moment also becomes singular at the origin of the parameter space defined by $(\hbar v_f k_x, \hbar v_f k_y, \Delta)$, i.e., at $(\hbar v_f k_x, \hbar v_f k_y, \Delta) = (0, 0, 0)$. But unlike the Berry curvature, the flux of an orbital magnetic moment vector field over a closed surface in the parameter space cannot be associated with a topological invariant. The orbital magnetic moment is inversely proportional to the energy ϵ_s [the radius of the closed spherical surface S in the parameter space defined by $(\hbar v_f k_x, \hbar v_f k_y, \Delta)$], i.e., $\vec{m}_z \propto \cos\theta\hat{z}/\epsilon_s$ [found using $(\hbar v_f k_x, \hbar v_f k_y, \Delta) = (\epsilon_s \sin\theta\cos\phi, \epsilon_s \sin\theta\sin\phi, \epsilon_s\cos\theta)$ in Eq. (30)]. This results in a flux of m_z over the surface S, which is directly proportional to the radius ϵ_s of the closed spherical surface S. Hence, as this flux changes with change in the size of the surface S, topologically it cannot be associated with a topological invariant (see Refs. [32,38] for topological invariant). Like the Berry curvature, in the absence of electromagnetic radiation, the orbital magnetic moment also exhibits threefold rotation symmetry in the momentum space both in the presence and absence of the band gap (Δ), see Figs. 8(a) and 8(d). Here also the presence of electromagnetic radiation (i.e., $a \neq 0$) breaks this threefold rotation symmetry [see Figs. 8(b) and 8(c)] and shifts the position of the orbital magnetic moment peak in the momentum space [see Figs. 8(e) and 8(f)].

In the crystalline materials having nonzero Berry curvature, the Bloch electrons thus exhibit the following equilibrium orbital magnetization:

$$M(\theta,a)=\frac{1}{4\pi^2}\sum_{s=\pm}\iint\bigg[f_{\rm eq}(\epsilon_s)\,m_{z,s}(k_x,k_y,\theta)+\frac{ek_BT}{\hbar}\Omega_s(k_x,k_y,\theta)\ln(1+e^{-(\epsilon_s-\mu)/k_BT})\bigg]\,dk_xdk_y, \tag{31}$$

where in Eq. (31) the first term is the magnetization arising due to the statistical sum of the orbital magnetic moment $m_{z,s}(k_x,k_y,\theta)$ [Eq. (29)] and the second term is the correction in the magnetization induced by the nonzero Berry curvature [18,30] [Eq. (17)]. The sum in Eq. (31) is on the conduction and valence band. Thus, the orbital magnetization occurs due to both orbital magnetic moment and Berry curvature (intrinsic property of Bloch states). In the absence of radiation (for $a=0$), the m_z and Ω_s are nonzero either for nonzero band gap (Δ) or hexagonal warping (λ_h), hence leading to a nonzero magnetization. But the magnetization can also be generated via irradiation only, for the case of linearly polarized off-resonant irradiation, the m_z and Ω_s are induced due to Fermi surface deformation produced by the anisotropic coupling of radiation with Dirac states in the Brillouin zone (i.e., m_z, $\Omega_s \neq 0$ even for $\Delta = 0$). In contrast, the circularly polarized light induces magnetization by the generation of time reversal symmetry breaking band gap in the energy spectrum [14]. The orbital magnetization $M(\theta,a)$ has periodic sinusoidal variation with the change in angle of polarization θ, see Fig. 9(a) [calculated using Eq. (31)]. Furthermore, it decreases as the electric field amplitude of the radiation is increased [see Fig. 9(b)]. This behavior of magnetization is a consequence of the presence of S_z spin component in the surface states of the topological insulator which shows exactly the same variation with change in a [see Fig. 4(d)]. This can be understood from Eqs. (29) and (17) that both m_z and Ω_z become zero as band gap (Δ) and hexagonal warping (λ_h) are made zero which corresponds to the absence of S_z spin component in the surface states (see Sec. II B for a detailed discussion).

Furthermore, the modification of Fermi surface shape by the hexagonal warping and the radiation has a significant effect on the orbital magnetization in the conduction and valence band. The variation of the orbital magnetization in the conduction and valence band is shown in Fig. 9(c) in the absence and presence of hexagonal warping and radiation. In the absence of hexagonal warping [see black dotted curve in Fig. 9(c)], the orbital magnetization has greater value than the case in which the Fermi surface is hexagonally warped [see blue curve in Fig. 9(c)], in both conduction and valence band. The orbital magnetization shows almost no variation with the change of chemical potential in both conduction and valence band. Whereas as the hexagonal warping in the Fermi surface is introduced, the orbital magnetization decreases as we rise up in the conduction band and deep down in the valence band [see blue curve in Fig. 9(c)]. The orbital magnetization further decreased as the topological insulator surface is irradiated with the linearly polarized electromagnetic radiation [see red and green curve in Fig. 9(c)], which is due to additional deformation of the Fermi surface by the radiation besides the deformation by the hexagonal warping. The orbital magnetization switches sign as we move from conduction band to valence band. This is because of the dominance of magnetization due to Berry curvature [second term of Eq. (31), which changes sign between the conduction and valence band] over

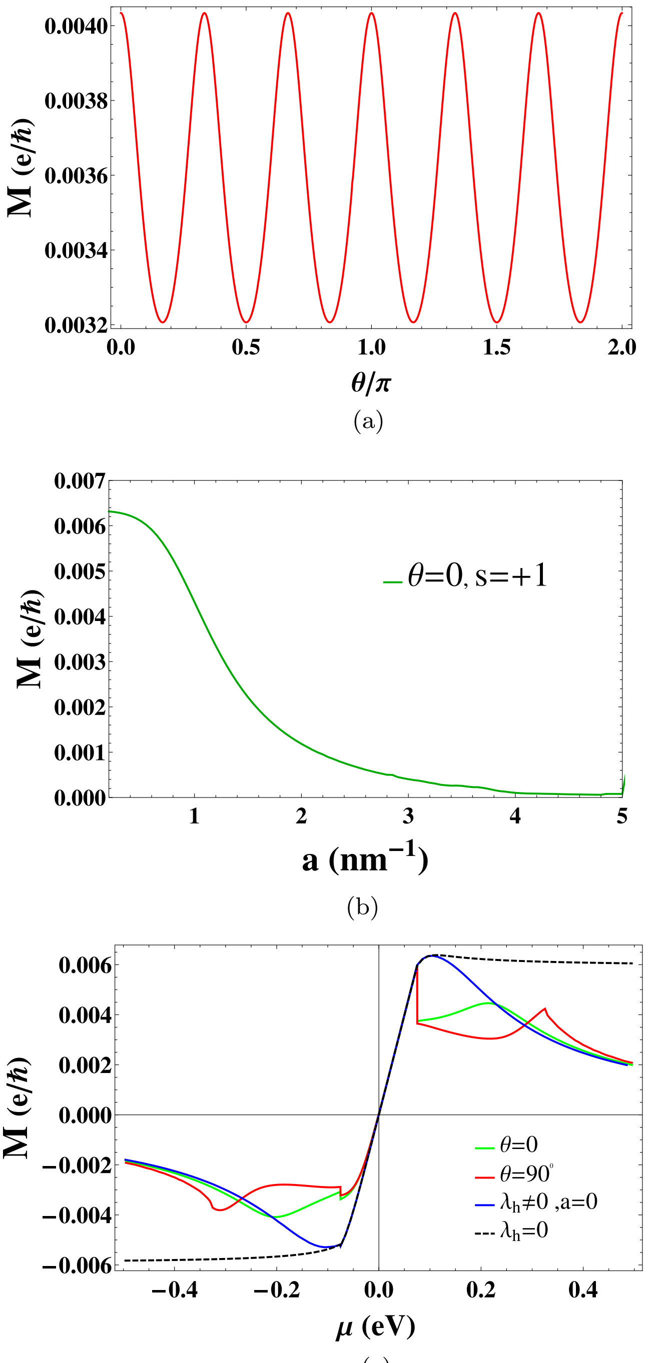

(a)

(b)

(c)

FIG. 9. The total orbital magnetization (M) is shown in (a)–(c) as a function of (a) the polarization angle θ, (b) the parameter a, and (c) the chemical potential μ.

the magnetization due to orbital magnetic moment [first term of Eq. (31), which does not change sign between conduction and valence band].

V. ANOMALOUS THERMOELECTRIC CONDUCTIVITIES

The nonzero Berry curvature leads to anomalous group velocity of the Bloch electron [18,30] and manifests itself as a correction in the orbital magnetization of the Bloch electrons in the crystalline material [18,30]. This Berry curvature modified orbital magnetization generates anomalous electronic and thermal currents (e.g., Nernst and Ettingshausen current) in the presence of statistical forces induced by the gradient of the chemical potential and temperature in ferromagnetic materials, topological insulators, and topological Weyl semimetals [14,18,39,40]. In this section we discuss the effect of the hexagonal warping of the Fermi surface of TI on the anomalous transverse Nernst, Ettingshausen, and thermal conductivities of the topological insulator irradiated with linearly polarized electromagnetic radiation.

A. Anomalous Ettingshausen thermal conductivity

For nonzero Berry curvature $\vec{\Omega}_s$, according to the theory of Ettingshausen effect, an anomalous transverse thermal current can be generated when a longitudinal electric field is applied on the surface of the topological insulator [18]. Consider a static electric field E_y applied in the y direction on the surface of the topological insulator which generates a heat current $j_{Q,x}$ in the x direction given by [18]

$$j_{Q,x} = \kappa_{xy}^{E} E_y. \tag{32}$$

κ_{xy}^{E} is the anomalous Ettingshausen transverse thermal conductivity given by [18,41]

$$\kappa_{xy}^{E} = \frac{e}{\hbar}\int \Omega(\vec{k})[(\epsilon-\mu)f_{\rm eq}+k_BT\ln(1+e^{-(\epsilon-\mu)/k_BT})]\frac{d^2\vec{k}}{(2\pi)^2}, \tag{33}$$

where, for the energy ϵ_s [Eq. (13)] and the Berry curvature $\vec{\Omega}_s$ [Eq. (17)], we can write the above equation in the following form:

$$\kappa_{xy}^{E}(\theta,a,\mu,T) = \frac{ek_BT}{2\pi h}\sum_{s=\pm}\iint \Omega_s(\theta,\alpha,k)\left[\frac{(\epsilon_s-\mu)f_{\rm eq}}{k_BT} + \ln(1+e^{-\frac{(\epsilon_s-\mu)}{k_BT}})\right]k\,dk d\alpha. \tag{34}$$

For qualitative analysis, we determine the κ_{xy}^{E} in the low temperature limit as we find for σ_{xy}. We use Mott relation $\kappa_{xy}^{E} = (\pi^2k_B^2T^2/3e)d\sigma_{xy}(\mu)/d\mu$ [18] to obtain the κ_{xy}^{E} in the low temperature limit $T\to 0$, Eq. (34) becomes

$$\kappa_{xy}^{E} = \frac{\pi^2}{3}\frac{ek_B^2T^2}{2\pi h}\sum_{s=\pm}\iint \Omega_s(\theta,\alpha,k)\delta(\mu-\epsilon_s)k\,dk d\alpha. \tag{35}$$

Equation (35) can be solved analytically for the Berry curvature in the absence of hexagonal warping given in Eq. (17), for which we find $\kappa_{xy}^{E} = -s(\pi^2k_B^2T^2/3e)\Delta/\mu^2$ in the conduction $(s=+)$ and valence $(s=-)$ band. From this we conclude that the κ_{xy}^{E} have opposite sign in the conduction and valence band and it is inversely proportional to the square of μ in both bands. This means the κ_{xy}^{E} decreases at a faster rate than σ_{xy} as we move deeper into the conduction or valence band. Besides this, the κ_{xy}^{E} attains maximum value at $|\mu| = \Delta$ (i.e., at the top of the valence band and the bottom of the conduction band). For μ in the band gap the κ_{xy}^{E} is found to be zero.

To understand the variation of the κ_{xy}^{E} at $T>0$, we calculated κ_{xy}^{E} numerically, using Eq. (34), as a function of θ, electric field amplitude parameter a, temperature T, and chemical potential μ. Figure 10 is plotted for the same parameter values as the plots of Fig. 7. Figure 10(a) shows that the Ettingshausen transverse thermal conductivity κ_{xy}^{E} varies sinusoidally with the polarization angle θ of the linearly polarized electromagnetic radiation. This sinusoidal variation can be thought of as a consequence of the direct dependence of κ_{xy}^{E} on the θ dependent Berry curvature $\vec{\Omega}_s$ [Eq. (17)]. The conductivity κ_{xy}^{E} as a function of the electric field amplitude parameter a is shown in Fig. 10(b), for the polarization angle $\theta=\pi/2$. The magnitude of the thermal conductivity $|\kappa_{xy}^{E}|$ decreases as the amplitude of the electric field is increased [see Fig. 10(b)]. At low amplitudes of the electric field, i.e., low value of a, the $|\kappa_{xy}^{E}|$ has a greater value as compared to the value at high values of a. Furthermore, the $|\kappa_{xy}^{E}|$ saturates to a constant value for high values of electric field amplitude.

Figures 10(a) and 10(b) imply that the thermal conductivity κ_{xy}^{E} can be controlled by tuning its polarization angle θ as well as the amplitude of the linearly polarized electromagnetic radiation. This control over the thermal conductivity κ_{xy}^{E} using θ and the amplitude of the electric field for the linearly polarized electromagnetic off-resonant irradiation of the topological insulator is possible only because of the presence of the hexagonal warping of the energy band of the topological insulator, which couples the electromagnetic radiation to the electronic momentum in the Hamiltonian [see Eq. (9)] and leads to a radiation parameter (polarization and amplitude) dependency. This is in contrast to the circularly polarized light off-resonant irradiation of the topological insulator for which the effect of radiation on the electrical and thermal conductivity can also be seen in the absence of hexagonal warping of the energy band structure [13,14].

To study how the presence of hexagonal warping in the energy band affects the thermal conductivity κ_{xy}^{E} can be seen from Fig. 10(c). Figure 10(c) shows the variation of κ_{xy}^{E} with chemical potential μ. Figure 10(c) shows that the thermal conductivity κ_{xy}^{E} has a smaller value for the case when there is no hexagonal warping (black dotted curve) than the case for which the hexagonal warping is nonzero (blue curve) in both the conduction and valence band, respectively. The conductivity κ_{xy}^{E} [Eq. (34)] is determined by the sum over the states on the Fermi surface and the Berry curvature Ω_s (which intrinsically encodes the spin texture information of the surface states u_α^0), hence this change in the κ_{xy}^{E} on introduction of hexagonal warping is the result of modification of both the shape of the Fermi surface and the spin texture of surface states, as it is for σ_{xy}. As shown in Fig. 10(c) (black and blue curve) κ_{xy}^{E} changes if the hexagonal warping goes from zero to nonzero. However, this change is not very large because the hexagonal warping in the Bi-chalcogenides topological insulators is essentially a k-cubic perturbation to the low

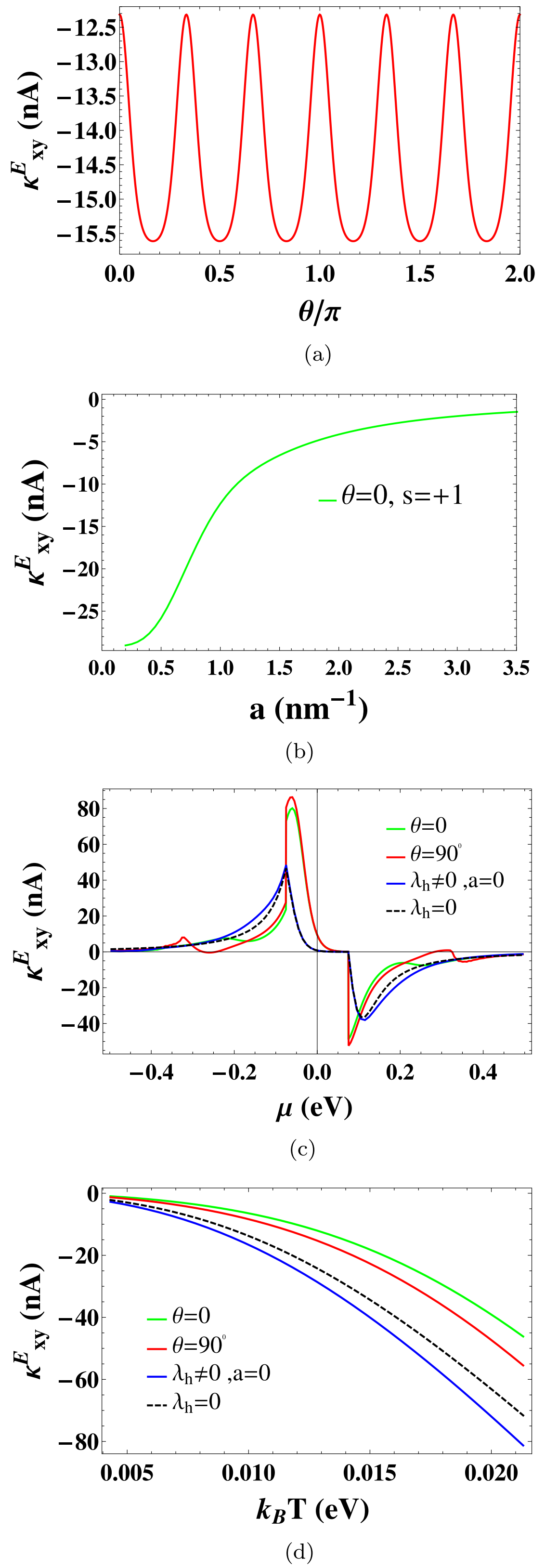

FIG. 10. The figures show the variation in the anomalous Ettingshausen thermal conductivity κ^E_{xy} with (a) the polarization angle θ, (b) the electric field amplitude parameter a, (c) the chemical potential μ, and (d) the temperature.

energy linear band structure of the surface states. The effects of modification of Fermi surface shape and spin texture on the change in thermal conductivity κ^E_{xy} are more pronounced in the presence of electromagnetic radiation (for $a \neq 0$ and $\lambda_h \neq 0$). This can be seen from Fig. 10(c) that the Ettingshausen thermal conductivity κ^E_{xy} is either greater or lesser [green and red curves in Fig. 10(c)] than the thermal conductivity for the case of hexagonal warping without electromagnetic radiation (i.e., $a = 0$ and $\lambda_h \neq 0$, blue curve). There are also kinks in the plots of the conductivity κ^E_{xy} in the presence of radiation [see Fig. 10(c) green and red curves] for the chemical potential in the range $0.3 < |\mu| < 0.4$. These kinks are the result of transition of the Fermi surface contour shape from one form to another in the energy range $0.3 < \epsilon_s < 0.4$ eV [see contours in this energy range in Fig. 2(d)].

Furthermore, similar to σ_{xy}, the conductivity κ^E_{xy} for all the cases also decreases to zero as we move deeper into the conduction band or valence band [see Fig. 10(c) for high positive and low negative values of μ]. Which can be explicitly understood as the inverse dependence of κ^E_{xy} on μ^2 at temperature $T = 0$ with inclusion of thermal brocading effect of $\delta(\mu - \epsilon_s)$ at temperature $T > 0$. We have also calculated the thermal conductivity κ^E_{xy} as a function of temperature, which is plotted in Fig. 10(d), for the temperature range of 50 to 200 K taken in units of $k_B T$, where k_B is the Boltzmann constant. Figure 10(d) shows that $|\kappa^E_{xy}|$ monotonically increases with the increase in the temperature T for all three cases (i) without hexagonal warping (black dotted curve), (ii) with hexagonal warping in the absence of electromagnetic field (blue curve), and (iii) with hexagonal warping in the presence of electromagnetic field (green and red curve).

B. Anomalous transverse Nernst and thermal conductivities due to a temperature gradient

Now, if instead of electric field E_y we have a temperature gradient $\nabla_y T$ in the y direction across the topological insulator surface developed using a cold and hot electrode. Then there will be a generation of a transverse electric current $j_{e,x}$ in the x direction due to the inverse Ettingshausen effect or Nernst effect. This is in contrast to the Ettingshausen effect where there is a generation of transverse heat current due to the electric field [Eq. (34)]. The Nernst electrical current is given by [18]

$$j_{e,x} = -\alpha_{xy} \nabla_y T, \tag{36}$$

α_{xy} is the anomalous transverse Nernst electrical conductivity given by [18]

$$\alpha_{xy} = \frac{\kappa^E_{xy}}{T}. \tag{37}$$

The behavior of the anomalous Nernst conductivity α_{xy} as a function of θ, electric field amplitude parameter a, temperature T, and chemical potential μ is the same as the behavior of κ^E_{xy} with the only difference that its magnitude is rescaled by the temperature T. Hence we have not plotted the figures for the Nernst conductivity α_{xy} here. In addition to the Nernst electric current induced by the temperature gradient, there is also the generation of a transverse heat current due to the temperature gradient which is given by the following equation:

$$j_{Q,x} = -\kappa_{xy} \nabla_y T, \tag{38}$$

where the κ_{xy} is the anomalous transverse thermal conductivity given by [18,42,43]

$$\kappa_{xy} = \frac{k_B^2 T}{h} \int \Omega(\vec{k}) \bigg[\frac{\pi^2}{3} + \left(\frac{\epsilon - \mu}{k_B T} \right)^2 f_{\rm eq} - 2Li_2(1 - f_{\rm eq}) \\ - [\ln(1 + e^{-(\epsilon-\mu)/k_B T})]^2 \bigg] \frac{d^2\vec{k}}{(2\pi)^2}. \tag{39}$$

In Eq. (39) the Li_2 is the polylogarithm function of order 2. The κ_{xy} can be calculated by using the Berry curvature given in Eq. (17) which modifies Eq. (39) to

$$\kappa_{xy}(\theta, a, \mu, T) = \frac{k_B^2 T}{4\pi^2 h} \sum_{s=\pm} \iint \Omega_s(\theta, \alpha, k) \bigg[\left(\frac{\epsilon_s - \mu}{k_B T} \right)^2 f_{\rm eq} \\ - 2Li_2(1 - f_{\rm eq}) - [\ln(1 + e^{-(\epsilon_s-\mu)/k_B T})]^2 \\ + \frac{\pi^2}{3} \bigg] k \, dk d\alpha. \tag{40}$$

The thermal conductivity κ_{xy} can be found at low temperature using the Mott relation $\kappa_{xy} = (\pi^2 k_B^2 T / 3e^2)\sigma_{xy}$, where the Hall conductivity σ_{xy} is given by Eq. (27), which implies at low temperature the thermal conductivity κ_{xy} differs from the Hall conductivity only by the constant factor and it is similar to the Hall conductivity σ_{xy}, it also depends upon the number of filled bands. We have plotted the thermal conductivity κ_{xy} as a function of angle θ, a, μ, and temperature T in Fig. 11. Just like the Hall conductivity σ_{xy} and Ettingshausen thermal conductivity κ_{xy}^E, the thermal conductivity κ_{xy} also varies sinusoidally with θ [see Fig. 11(a)] and monotonically decreases with the increase in the amplitude of the electric field of linearly polarized electromagnetic radiation [see Fig. 11(b)]. Similar to κ_{xy}^E, the κ_{xy} also saturates to zero at high values of electric field amplitude. The variation of thermal conductivity κ_{xy} with chemical potential μ is shown in Fig. 11(c). In contrast to the Ettingshausen thermal conductivity κ_{xy}^E [see Fig. 10(c)], in both the conduction and valence band, the thermal conductivity κ_{xy} is found to be greater in the absence of hexagonal warping [black dotted curve, Fig. 11(c)] than in the case of the presence of hexagonal warping without irradiation [blue curve Fig. 11(c)]. In the presence of hexagonal warping, κ_{xy} gets further reduced when the topological insulator surface is irradiated with linearly polarized radiation [see red and green curves in Fig. 11(c)]. Similar to Hall conductivity σ_{xy}, κ_{xy} decreases as we move up in the conduction band and moves down in the valence band because they both depend upon how much the states of the valence and conduction bands are occupied (i.e., fully filled or fully vacant energy bands do not lead to nonzero conductivities). In contrast to κ_{xy}^E, the κ_{xy} is positive in both the valence and conduction bands. The κ_{xy} also increases with an increase in temperature both in the presence and absence of radiation [see Fig. 11(d)].

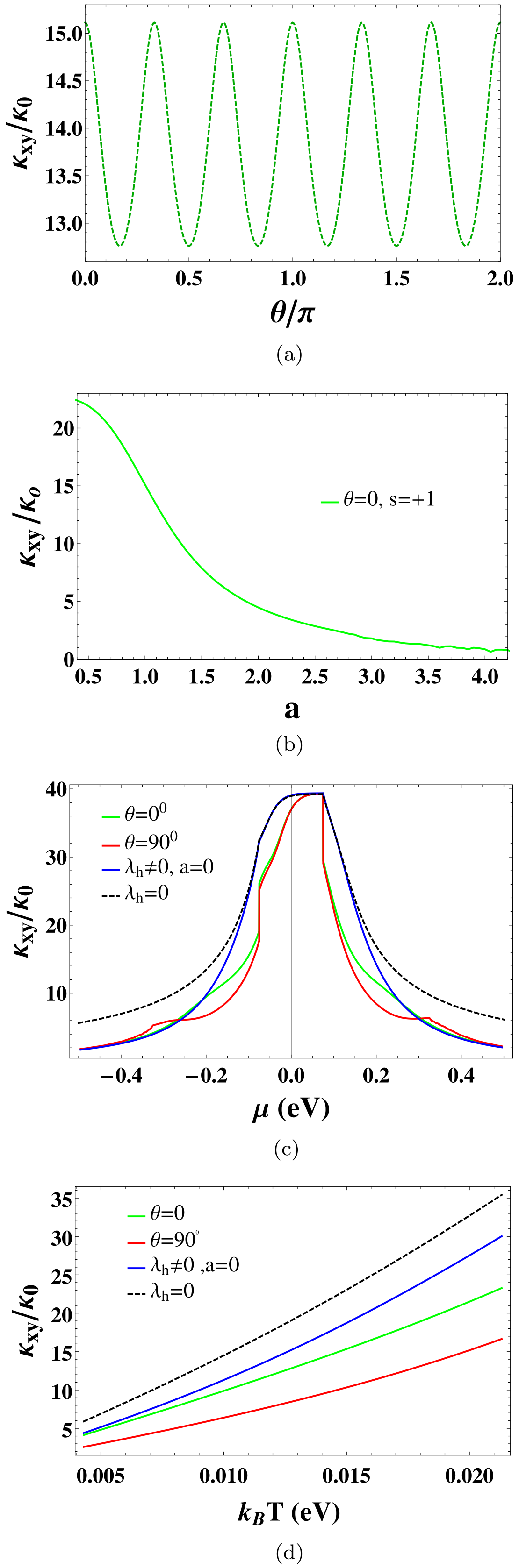

(a)

(b)

(c)

(d)

FIG. 11. The anomalous thermal conductivity k_{xy} is shown in (a)–(d) as a function of (a) the polarization angle θ, (b) the parameter a, (c) the chemical potential μ, and (d) the temperature.

VI. FIGURE OF MERIT, *ZT* PARAMETER

How effectively a thermoelectric material converts heat into electricity is determined by the coefficient of performance

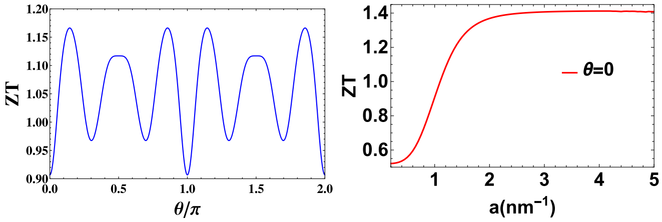

(a) (b)

FIG. 12. The figure shows variation in figure of merit (ZT) with (a) the polarization angle θ and (b) the parameter a. ZT in these figures is calculated for $\mu = 0.15$ eV.

or the figure of merit (ZT) given by $ZT = \sigma\, S^2\, T/(\kappa_e + \kappa_l)$. Where S, σ, κ_e, and κ_l define the Seebeck power, Hall electric conductivity, electronic thermal conductivity, and lattice-thermal conductivity [44,45], respectively, and T is the temperature. Both bulk and surface states contribute to thermoelectric efficiency of the topological insulator. But for the topological insulator thin films, enhancement in the ZT has been reported due to a significant increase in surface states contribution to the electrical conductivity σ and Seebeck coefficient S and due to suppression in the lattice-thermal conductivity (i.e .,$\kappa_l \ll \kappa_e$). So, for the topological insulator thin film, the figure of merit because of the surface states is given by [44–48]

$$ZT = \frac{\sigma_s\, S_s^2\, T}{\kappa_{e,s}}, \tag{41}$$

where $\sigma_s = \sigma_{xx}$, $S_s = S_{xx} = (\sigma_{yy}\alpha_{xx} + \sigma_{xy}\alpha_{xy})/(\sigma_{xx}\sigma_{yy} + \sigma_{xy}^2)$, and $\kappa_{e,s} = \kappa_{xx} = \mathcal{L}_x^2/T - S_{xx}^2\sigma_{xx}$ [45]. To determine these quantities we use Onsager relations given by $\sigma_{ii} = e^2\mathcal{L}_i^0$ and $\alpha_{ii} = e\mathcal{L}_i^1/T$, where we have [45]

$$\mathcal{L}_i^n = \sum_{s=\pm}\int \frac{d^2 k}{(2\pi)^2}\left(-\frac{\partial f_{\rm eq}}{\partial \epsilon_s}\right)\tau(\epsilon_s)\left(\frac{1}{\hbar}\frac{\partial \epsilon_s}{\partial k_i}\right)^2(\epsilon_s - \mu)^n, \tag{42}$$

with $n = 0, 1, 2$, $i = x, y$, and $\tau(\epsilon_s)$ as the relaxation time. The above longitudinal conductivities have been calculated under constant relaxation time approximation [49,50] for which we use $\tau(\epsilon_s) = \tau = 22$ fs [51] for TI. The figure of merit ZT is calculated using Eq. (41) for $\mu = 0.15$ eV which on one hand shows nonsinusoidal dependence with variation in the angle of polarization θ [see Fig. 12(a)]. On the other hand, there is a significant enhancement in the value of figure of merit ZT from the 0.6 to 1.4 as we increase the value radiation amplitude parameter a [see Fig. 12(b)]. This value of ZT in the presence of LP radiation is larger than the case of the presence of hexagonal warping and the absence of LP radiation for which ZT is equal to 0.52. The value $ZT = 0.52$ is not very large as compared to the case of the absence of both hexagonal warping and LP radiation for which we have found to be $ZT = 0.39$ [48]. This enhancement strongly indicates the possible linearly polarized electromagnetic radiation parameter controllable thermoelectric application of the topological insulator for the conversion of heat into electricity.

It is important to note here that our results are valid for temperatures less than the Debye temperature of the topological insulator. The Debye temperature of the $\mathrm{Bi_2Se_3}$ topological insulator is around 182–185 K [52,53] and we use the temperature $T = 150$ K for the calculation of the transverse Nernst, Ettingshausen, and thermal conductivities. For temperatures above the Debye temperature the electron-phonon coupling effects have a pronounced effect on the transport of the Dirac electron on the surface of the topological insulator, which are negligible for the temperatures below the Debye temperatures [54]. Hence for calculation of these conductivities for the temperature above the Debye temperature the electron-phonon coupling must be included in the model [55].

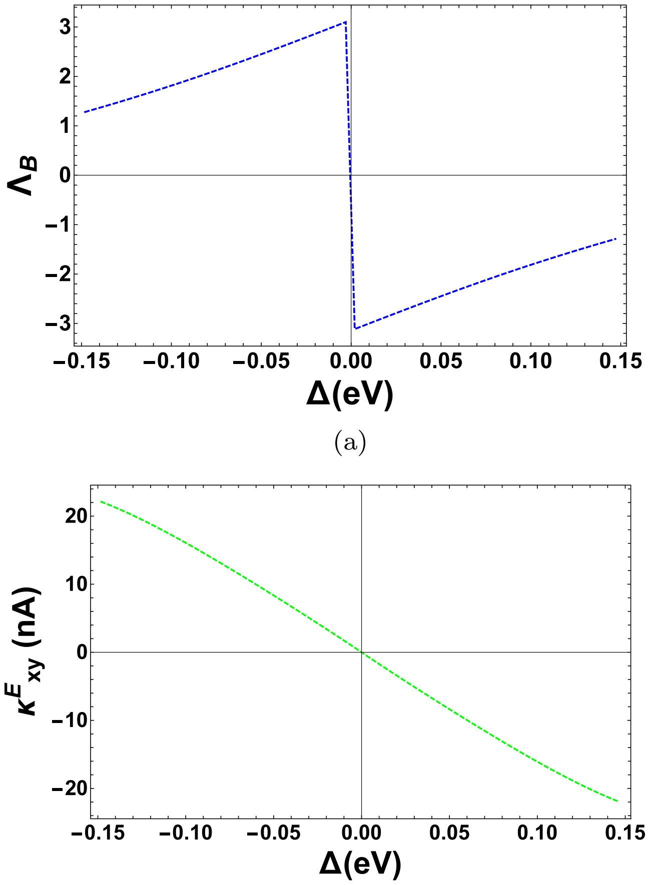

(a)

(b)

FIG. 13. The figure shows (a) Berry phase variation with Δ and (b) Ettingshausen conductivity (κ_{xy}) variation with Δ.

VII. CONCLUSIONS

In summary, we studied the effect of the hexagonal warping of the Fermi surface on the anomalous thermoelectric properties of the topological insulator surface irradiated with linearly polarized electromagnetic off-resonant radiation. We have found that the off-resonant linearly polarized (LP) irradiation induces Floquet-Dirac states on the surface of the topological insulator only in the presence of hexagonal warping of the Fermi surface. Interestingly, in the presence of hexagonal warping, the Berry curvature, spin texture, and orbital magnetization associated with surface states induced by the LP radiation are found to have strong dependence on angle of polarization and have broken C_3 symmetry in the Brillouin zone, which are otherwise C_3 symmetric in the absence of LP irradiation. This broken C_3 symmetry of Berry curvature leads to Berry phase which varies sinusoidally with angle of polarization and monotonically increases with an increase in amplitude of the LP radiation.

Furthermore, we conclude that both the modification of the spin texture and Fermi surface by the linearly polarized radiation, in addition to the effects produced by the hexagonal warping, lead to LP radiation polarization angle and electric field amplitude controllable anomalous Nernst, Ettingshausen, and thermal transverse conductivities. These conductivities have been found to vary sinusoidally with polarization angle and decrease with an increase in the amplitude of radiation in both conduction and valence band. Both the anomalous Nernst and Ettingshausen transverse conductivities have opposite signs in the conduction and valence band. However, the anomalous transverse thermal conductivity has the same sign in both the conduction and valence bands. The variation in these conductivities with radiation parameter collectively leads to enhancement in the value of the figure of merit (ZT). We show ZT varies sinusoidally with θ and increases significantly from 0.6 to 1.4 as the amplitude of radiation increases. Hence, we expect that these linearly polarized radiation parameter controllable anomalous thermoelectric conductivities of the topological insulator may find important technological applications for the conversion of heat into electricity or vice versa in thermoelectronics.

ACKNOWLEDGMENTS

T.C. would like to thank the University Grants Commission (UGC) for a Senior Research Fellowship (SRF). N.D. would like to thank the University of Delhi R & D Grant, Department of Science and Technology Government of India (SERB grant EMR/2016/006536) and ICTS for faculty associateship.

APPENDIX: RESULTS FOR $\Delta < 0$

In this Appendix we have shown a few results for the negative value of Δ. All the results shown in the above sections are for Δ having a positive value but it is also possible to have a negative value of Δ. The band gap parameter Δ varies with thickness of the topological insulator thin film. The Δ sign is to be positive for the film thickness less than 25 Å and negative for the film thickness in between 25 and 32 Å range [25,26]. We calculated thermoelectric conductivities for the negative value of Δ also. We find all the physical quantities calculated in this paper change sign with the change in the sign of Δ. As shown in Figs. 13(a) and 13(b), the Berry phase and Ettingshausen transverse conductivities change sign as the sign of Δ is changed.

[1] B. M. Fregoso, Y. H. Wang, N. Gedik, and V. Galitski, Phys. Rev. B **88**, 155129 (2013).

[2] N. H. Lindner, G. Refael, and V. Galitski, Nat. Phys. **7**, 490 (2011).

[3] J. Cayssol, B. Dora, F. Simon, and R. Moessner, Phys. Status Solidi (RRL) **7**, 101 (2013).

[4] T. Oka and H. Aoki, Phys. Rev. B **79**, 081406(R) (2009).

[5] T. Kitagawa, E. Berg, M. Rudner, and E. Demler, Phys. Rev. B **82**, 235114 (2010).

[6] Y. H. Wang, H. Steinberg, P. Jarillo-Herrero, and N. Gedik, Science **342**, 453 (2013).

[7] A. Junck, G. Refael, and F. von Oppen, Phys. Rev. B **88**, 075144 (2013).

[8] H. Plank, L. E. Golub, S. Bauer, V. V. Bel'kov, T. Herrmann, P. Olbrich, M. Eschbach, L. Plucinski, C. M. Schneider, J. Kampmeier, M. Lanius, G. Mussler, D. Grützmacher, and S. D. Ganichev, Phys. Rev. B **93**, 125434 (2016).

[9] Y. G. Semenov, X. Li, and K. W. Kim, Phys. Rev. B **86**, 201401(R) (2012).

[10] J. D. Yao, J. M. Shao, S. W. Li, D. H. Bao, and G. W. Yang, Sci. Rep. **5**, 14184 (2015).

[11] F. D. M. Haldane, Phys. Rev. Lett. **61**, 2015 (1988).

[12] H. L. Calvo, L. E. F. Foa Torres, P. M. Perez-Piskunow, C. A. Balseiro, and G. Usaj, Phys. Rev. B **91**, 241404(R) (2015).

[13] X. Zhou, Y. Xu, and G. Jin, Phys. Rev. B **92**, 235436 (2015).

[14] M. Tahir and P. Vasilopoulos, Phys. Rev. B **91**, 115311 (2015).

[15] J. W. McIverJ, D. Hsieh, H. Steinberg, P. Jarillo-Herrero, and N. Gedik, Nat. Nano **7**, 96 (2012).

[16] J. Sánchez-Barriga, E. Golias, A. Varykhalov, J. Braun, L. V. Yashina, R. Schumann, J. Minár, H. Ebert, O. Kornilov, and O. Rader, Phys. Rev. B **93**, 155426 (2016).

[17] P. Hosur, Phys. Rev. B **83**, 035309 (2011).

[18] D. Xiao, Y. Yao, Z. Fang, and Q. Niu, Phys. Rev. Lett. **97**, 026603 (2006).

[19] H. J. Goldsmid, *Introduction to Thermoelectricity* (Springer, Berlin, 2010).

[20] L. Fu, Phys. Rev. Lett. **103**, 266801 (2009).

[21] C.-X. Liu, X.-L. Qi, H. J. Zhang, X. Dai, Z. Fang, and S.-C. Zhang, Phys. Rev. B **82**, 045122 (2010).

[22] Y. L. Chen, J. G. Analytis, J.-H. Chu, Z. K. Liu, S.-K. Mo, X. L. Qi, H. J. Zhang, D. H. Lu, X. Dai, Z. Fang, S. C. Zhang, I. R. Fisher, Z. Hussain, and Z.-X. Shen, Science **325**, 178 (2009).

[23] K. W. Kim, T. Morimoto, and N. Nagaosa, Phys. Rev. B **95**, 035134 (2017).

[24] Z. Li and J. P. Carbotte, Phys. Rev. B **89**, 165420 (2014).

[25] H.-Z. Lu, W.-Y. Shan, W. Yao, Q. Niu, and S.-Q. Shen, Phys. Rev. B **81**, 115407 (2010).

[26] Y. Zhang, K. He, C.-Z. Chang, C.-L. Song, L.-L. Wang, X. Chen, J.-F. Jia, Z. Fang, X. Dai, W.-Y. Shan *et al.*, Nat. Phys. **6**, 584 (2010).

[27] T. Kitagawa, T. Oka, A. Brataas, L. Fu, and E. Demler, Phys. Rev. B **84**, 235108 (2011).

[28] R. Wang, B. Wang, R. Shen, L. Sheng, and D. Y. Xing, Europhys. Lett. **105**, 17004 (2014).

[29] D. A. Lovey, G. Usaj, L. E. F. Foa Torres, and C. A. Balseiro, Phys. Rev. B **93**, 245434 (2016).

[30] M.-C. Chang and Q. Niu, Phys. Rev. B **53**, 7010 (1996).

[31] D. Xiao, M.-C. Chang, and Q. Niu, Rev. Mod. Phys. **82**, 1959 (2010).

[32] S. Shen, *Topological Insulators: Dirac Equation in Condensed Matter*, Springer Series in Solid-State Sciences (Springer, Singapore, 2017).

[33] M. V. Berry, Proc. R. Soc. London Ser. A **392**, 45 (1984).

[34] D. Hsieh, Y. Xia, L. Wray, D. Qian, A. Pal, J. H. Dil, J. Osterwalder, F. Meier, G. Bihlmayer, C. L. Kane, Y. S. Hor, R. J. Cava, and M. Z. Hasan, Science **323**, 919 (2009).

[35] H. Zhang, C.-X. Liu, and S.-C. Zhang, Phys. Rev. Lett. **111**, 066801 (2013).

[36] D. Hsieh, Y. Xia, D. Qian, L. Wray, J. Dil, F. Meier, J. Osterwalder, L. Patthey, J. Checkelsky, N. Ong *et al.*, Nature (Loindon) **460**, 1101 (2009).

[37] G. Sundaram and Q. Niu, Phys. Rev. B **59**, 14915 (1999).

[38] S. M. Bhattacharjee, Use of topology in physical problems, in *Topology and Condensed Matter Physics*, edited by S. M. Bhattacharjee, M. Mj, and A. Bandyopadhyay (Springer, Singapore, 2017), pp. 171–216.

[39] R. Lundgren, P. Laurell, and G. A. Fiete, Phys. Rev. B **90**, 165115 (2014).

[40] Q. Chen and G. A. Fiete, Phys. Rev. B **93**, 155125 (2016).

[41] T. Qin, Q. Niu, and J. Shi, Phys. Rev. Lett. **107**, 236601 (2011).

[42] D. L. Bergman and V. Oganesyan, Phys. Rev. Lett. **104**, 066601 (2010).

[43] T. Yokoyama and S. Murakami, Phys. Rev. B **83**, 161407(R) (2011).

[44] P. Ghaemi, R. S. K. Mong, and J. E. Moore, Phys. Rev. Lett. **105**, 166603 (2010).

[45] Y. V. Ivanov, A. T. Burkov, and D. A. Pshenay-Severin, Phys. Status Solidi (b) **255**, 1800020 (2018).

[46] M. Tahir, A. Manchon, and U. Schwingenschlögl, J. Appl. Phys. **116**, 093708 (2014).

[47] S. Murakami, R. Takahashi, O. A. Tretiakov, A. Abanov, and J. Sinova, J. Phys.: Conf. Series **334**, 012013 (2011).

[48] O. A. Tretiakov, A. Abanov, and J. Sinova, Appl. Phys. Lett. **99**, 113110 (2011).

[49] J. E. Cornett and O. Rabin, Phys. Rev. B **84**, 205410 (2011).

[50] H. Osterhage, J. Gooth, B. Hamdou, P. Gwozdz, R. Zierold, and K. Nielsch, Appl. Phys. Lett. **105**, 123117 (2014).

[51] T. J. Scheidemantel, C. Ambrosch-Draxl, T. Thonhauser, J. V. Badding, and J. O. Sofo, Phys. Rev. B **68**, 125210 (2003).

[52] X. X. Yang, Z. F. Zhou, Y. Wang, R. Jiang, W. T. Zheng, and C. Q. Sun, J. Appl. Phys. **112**, 083508 (2012).

[53] G. E. Shoemake, J. A. Rayne, and R. W. Ure, Phys. Rev. **185**, 1046 (1969).

[54] N. W. Ashcroft and N. D. Mermin, *Solid State Physics* (Harcourt College, London, 1976).

[55] H. Dehghani, T. Oka, and A. Mitra, Phys. Rev. B **90**, 195429 (2014).